

1 **Estimation of oceanic sub-surface mixing under a severe cyclonic storm**
2 **using a coupled atmosphere-ocean-wave model**

3 Kumar Ravi Prakash, Tanuja Nigam, Vimlesh Pant

4 Centre for Atmospheric Sciences, Indian Institute of Technology Delhi, New Delhi-110016

5
6 **Abstract**

7 A coupled atmosphere-ocean-wave model used to examine mixing in the upper oceanic
8 layers under the influence of a very severe cyclonic storm Phailin over the Bay of Bengal (BoB)
9 during 10-14 October 2013. Model simulations highlight prominent role of cyclone induced near-
10 inertial oscillations in sub-surface mixing up to the thermocline depth. The inertial mixing
11 introduced by the cyclone played a central role in deepening of the thermocline and mixed layer
12 depth by 40 m and 15 m, respectively. For the first time over the BoB, A detailed analysis of
13 inertial oscillation kinetic energy generation, propagation, and dissipation was carried out using
14 an atmosphere-ocean-wave coupled model during a cyclone. at a location in northwestern BoB.
15 The peak magnitude of kinetic energy in baroclinic and barotropic currents found to be $1.2 \text{ m}^2 \text{ s}^{-2}$
16 and $0.3 \times 10^{-2} \text{ m}^2 \text{ s}^{-2}$, respectively. The power spectrum analysis suggested a dominant frequency
17 operative in sub-surface mixing was associated with near inertial oscillations. The peak strength
18 of $0.84 \text{ m}^2 \text{ s}^{-1}$ in zonal baroclinic current found at 14 m depth. The baroclinic kinetic energy remain
19 higher ($> 0.03 \text{ m}^2 \text{ s}^{-2}$) during 11-12 October and decreased rapidly thereafter. The wave-number
20 rotary spectra identified the downward propagation, from surface up to the thermocline, of energy
21 generated by inertial oscillations. A quantitative analysis of shear generated by the near inertial
22 baroclinic current showed higher shear generation at 40-80 m depth during peak surface winds.
23 Analysis highlights that greater mixing within the mixed layer take place where the eddy kinetic
24 diffusivity was high ($> 6 \times 10^{-11} \text{ m}^2 \text{ s}^{-1}$). The turbulent kinetic energy dissipation rate increased from
25 4×10^{-14} to $2.5 \times 10^{-13} \text{ W kg}^{-1}$ on approaching the thermocline that dampened mixing process further
26 downward into the thermocline layer. A quantitative estimate of kinetic energy in the oceanic water
27 column, its propagation and dissipation mechanisms were explained using the coupled
28 atmosphere-ocean-wave model. The large shear generated by the inertial oscillations found to
29 overcome the stratification and initiate mixing at the base of the mixed layer. Greater mixing was
30 found at the depths where the eddy kinetic diffusivity was large. The baroclinic current, holding a

31 larger fraction of kinetic energy than the barotropic current, weakened rapidly after the passage of
32 cyclone. The shear-induced by inertial oscillations found to decrease rapidly with increasing depth
33 below the thermocline. The dampening of mixing process below the thermocline explained
34 through the enhanced dissipation rate of turbulent kinetic energy upon approaching the
35 thermocline layer. The wave-current interaction, non-linear wave-wave interaction were found to
36 affect the process of downward mixing and cause the dissipation of inertial oscillations.

39 **1. Introduction**

40 The Bay of Bengal (BoB), a semi-enclosed basin in the northeastern Indian ~~Ocean~~ocean,
41 consists of surplus near-surface fresh water due to large precipitation and runoff from the major
42 river systems of the Indian subcontinent (Varkey et al., 1996; Rao and Sivakumar, 2003; Pant et
43 al., 2015). Presence of fresh water leads to salt-stratified upper ocean water column and formation
44 of barrier layer (BL), a layer sandwiched between bottom of the mixed layer (ML) and top of the
45 thermocline, in the BoB (Lukas and Lindstrom, 1991; Vinayachandran et al., 2002; Thadathil et
46 al., 2007). The BL restricts entrainment of colder waters from thermocline region into the mixed
47 layer thereby, maintains warmer ML and sea surface temperature (SST). The warmer SST together
48 with higher tropical cyclone heat potential (TCHP) makes the BoB as one of the active regions for
49 cyclogenesis (Suzana et al. 2007; Yanase et al. 2012, Vissa et al. 2013). Majority of tropical
50 cyclones generate during the pre-monsoon (April-May) and post-monsoon (October-November)
51 seasons (Alam et al., 2003; Longshore, 2008). The number of cyclones and their intensity is highly
52 variable in seasonal and interannual time scales. ~~The stratification of the Ocean is one of the~~
53 ~~important factor to drive the ocean response of the tropical cyclone.~~ The oceanic response to the
54 tropical cyclone depends on the stratification of the ocean. The BL formation in the BoB is
55 associated with the strong stratification due to the peak discharge from rivers in the post-monsoon
56 season. The intensity of the cyclone largely depends on the degree of stratification (Neetu et al.
57 2012; Li et al. 2013). The coupled atmosphere-ocean model found to improve the intensity of
58 cyclonic storm when compared to the uncoupled model over different oceanic regions (Warner et
59 al., 2010; Zambon et al., 2014; Srinivas et al., 2016; Wu et al., 2016). Zambon et al. (2014)
60 compared the simulations from the coupled atmosphere-ocean and uncoupled models and reported

61 significant improvement in the intensity of storm in the coupled case as compared to the uncoupled
62 case. The uncoupled atmospheric model produced large ocean-atmosphere enthalpy fluxes and
63 stronger winds in the cyclone (Srinivas et al., 2016). When the atmospheric model WRF was
64 allowed interactions with the ocean model, the SST found to be more realistic as compared to
65 warm bias in the stand-alone WRF (Warner et al., 2010). Wu et al. (2016) demonstrated the
66 advantage of using a coupled model over the uncoupled model in better simulation of typhoon
67 Megi's intensity.

68 Mixing in the water column has an important role in energy and material transference.
69 Mixing in the ocean can be introduced by the different agents such as wind, current, tide, eddy,
70 and cyclone. Mixing due to tropical cyclones is mostly limited to the upper ocean but the cyclone-
71 induced internal waves can affect the subsurface mixing. Several studies have observed that the
72 mixing in the upper oceanic layer is introduced due to the generation of near-inertial oscillations
73 (NIO) during the passage of tropical cyclones (Gonella, 1971; Shay et al., 1989; Johanston et al.,
74 2016). This mixing is responsible for deepening of ML and shoaling of the thermocline (Gill,
75 1984). The vertical mixing caused by storm-induced NIO has a significant impact on the upper
76 ocean variability (Price, 1981). The NIO are also found to be responsible for the decrement of SST
77 along the cyclone track (Chang and Anthes, 1979; Leipper, 1967; Shay et al., 1992; Shay et al.,
78 2000). This decrease in SST is caused by the entrainment of cool subsurface thermocline water in
79 the mixed layer into the immediate overlying layer of water. This cooling of surface water is one
80 of the ~~component of the decaying mechanism of the stormy event~~ reason for the decay of cyclone
81 (Cione and Uhlhorn, 2003). There is a remarkable difference in the The magnitude of surface this
82 cooling ~~of surface temperature~~ differs largely depending on the degree of stratification at the
83 rightward to the cyclone track (Jacob, 2003; Price et al., 1981). ~~moving on the highly stratified to~~
84 ~~less or weakly stratified bay locations those are falling at the rightward to the cyclone track (Jacob,~~
85 ~~2003; Price et al., 1981).~~

86 The near-inertial process can be analyzed from the baroclinic component of currents. The
87 vertical shear of horizontal baroclinic velocities that is interrelated to buoyancy oscillations of
88 surface layers ~~are is~~ utilized in various studies to have an adequate understanding of the mixing
89 associated with high frequency oscillations i.e. NIO (Zhang et al., 2014). The shear generated due
90 to NIO is an ~~one of the~~ important factor ~~other than the wind stress~~ for the intrusion of the cold

91 thermocline water into the ML during near-inertial scale mixing (Price et al., 1978; Shearman,
92 2005; Burchard and Rippeth, 2009). The alternative upwelling and downwelling features of the
93 temperature profile are an indication of the inertial mixing. The Kinetic energy bounded with these
94 components of current shows a rise in magnitude at the right side of cyclone track (Price et al.,
95 1981; Sanfoard et al., 1987; Jacob, 2003). The reason for this high magnitude of kinetic energy is
96 linked with strong wind and rotating wind vector condition of the storm. The spatial distribution
97 of near-inertial energy is primarily controlled by the boundary effect for inertial oscillations (Chen
98 et al., 2017). The NIO energy found to decline with the decreasing depth and vanish in the coastal
99 regions (Schahinger, 1988; Chen et al., 2017).

100 In several studies (Chang et al., 2008; Lin et al., 2008; Shang et al., 2008; Lin et al., 2003;
101 Zhao et al., 2009), upper Ocean response for various cyclonic events is also inspected and proved
102 for the enhancement of primary productivity during post cyclone state of the Ocean. At the time
103 when storm is active and prior to it, the surface concentration of chlorophyll a (Chl a), a proxy for
104 the concentration of primary productivity is comparatively lower than that of the post cyclonic
105 state of ocean surface (Sarangi, 2011, Latha et al., 2015). This increment in the chlorophyll is
106 dependent on the relative entrainment of the cool subsurface water, enriched in nutrient under the
107 influence of energetic near inertial wave mixing caused by the tropical cyclones.

108 The Aimain of this paper is to understand and quantify the near-inertial mixing due to the
109 very severe cyclonic storm Phailin in the BoB, a very severe cyclonic storm (VSCS) in the BoB.
110 Phailin was developed over the BoB in the northern Indian ocean in October 2013. The landfall of
111 Phailin occurred on 12 October 2013 around 15:30 GMT near Gopalpur district of Odisha state on
112 the east coast of India. After the 1999 super cyclonic event of the Odisha coast, Phailin was the
113 second strongest cyclonic event that made landfall on the east coast of India (Kumar and Nair,
114 2015). The low-pressure system developed in the north of the Andaman Sea on 7th October 2013,
115 which transformed into a depression on 8th October at 12 °N, 96 °E. This depression got converted
116 to a cyclonic disturbance on 9th October and further intensified while moved to east-central BoB
117 and opted the maximum wind speed of 200 km h⁻¹ at 03:00 GMT on 11th October. Finally, landfall
118 occurs at 17:00 GMT 12th October. More details on the development and propagation of Phailin
119 can be found in the literature (IMD Report, 2013; Mandal et al. 2015). The performance of the

120 coupled atmosphere-ocean model in simulating the oceanic parameters temperature, salinity, and
121 currents during the Phailin is accessed in Prakash and Pant (2017).

122 Most of the past studies on the oceanic mixing under cyclonic conditions were carried out
123 using in-situ measurements, which are constrained by the spatial and temporal availability. To the
124 best of our knowledge, the present study is first of its kind that utilizes a coupled atmosphere-
125 ocean-wave model over the BoB to estimate the cyclone-induced mixing and associated energy
126 propagation at the cyclone track and a location of maximum surface wind stress during the period
127 of peak intensity of the cyclone. The study also focuses on analyzing the subsurface distribution
128 of NIO with its vertical mixing potential. Further, the study quantifies the shear generated mixing
129 and the kinetic energy of these baroclinic mode of horizontal current varying in the vertical section
130 at a selected location during the active period of the cyclone. The dissipation rate of NIO and
131 turbulent eddy diffusivity are quantified.

132

133 2. Data and Methodology

134 2.1 Model details

135 Numerical simulations during the period of ~~VSCS~~-Phailin were carried out using the
136 coupled ~~Ocean Atmosphere wave Sediment~~—ocean-atmosphere-wave-sediment transport
137 (COAWST), described in detail by Warner et al. (2010). COAWST modeling system couples the
138 three-dimensional oceanic model ‘Regional Ocean Modeling System’ (ROMS), the atmospheric
139 model ‘Weather Research and Forecasting’ (WRF), and the wind wave generation and propagation
140 model ‘Simulating Waves Nearshore’ (SWAN). ROMS model used for the study is a free surface,
141 primitive equation, sigma coordinate model. ROMS is a hydrostatic ocean model that solves finite
142 difference approximations of the Reynolds averaged Navier-~~S~~Stokes equations (~~e~~C~~h~~assignet et al.,
143 2000; Haidvogel et al., 2000, Haidvogel et al., 2008; Shchepetkin and McWilliams, 2005). The
144 atmospheric model component in the COAWST is a non-hydrostatic, compressible model
145 ‘Advanced Research Weather Research Forecast Model’ (WRF-ARW), described in Skamarock
146 et al., (2005). It has different schemes for representation of boundary layer physics and physical
147 parameterizations of sub-grid scale processes. In the COAWST modeling system, appropriate
148 modifications were made in the code of atmospheric model component to provide an improved

149 bottom roughness from the calculation of the bottom stress over the ocean (Warner et al., 2010).
150 Further, the momentum equation is modified to improve the representation of surface waves. The
151 modified equation needs the additional information of wave energy dissipation, propagation
152 direction, wave height, wave-length that are obtained from wave component of the COAWST
153 model.

154 The spectral wave model SWAN, used in the COAWST modeling system, is designed for
155 shallow water. The wave action balance equation is solved in the wave model for both spatial and
156 spectral spaces (Booij et al. 1999). ~~In the COAWST, the ocean model ROMS simulated free~~
157 ~~surface elevations (ELV), and current (CUR) are provided to the wave model SWAN. The Kirby~~
158 ~~and Chen (1998) formulation has been used for the computation of current. The Model Coupling~~
159 ~~Toolkit (MCT) used as a coupler in the COAWST modeling system to couple different model~~
160 ~~components (Larson et al., 2004; Jacob et al., 2005). A parallel-coupled approach is utilized by the~~
161 ~~coupler that permits the transmission and transformation of various distributed parameters between~~
162 ~~component models. MCT coupler facilitates exchanges of prognostic variables from one model to~~
163 ~~another model components. Further details on various parameters exchanged among the~~
164 ~~component models of COAWST modeling system can be found in Warner et al. (2010). The SWAN~~
165 ~~model used in the COAWST system includes the wave-wind generation, wave-breaking, wave-dissipation,~~
166 ~~and nonlinear wave-current-wind interaction. The ‘Model Coupling Toolkit’ (MCT) used as a coupler in~~
167 ~~the COAWST modeling system to couple different model components (Larson et al., 2004; Jacob et al.,~~
168 ~~2005). The coupler utilizes a parallel-coupled approach to facilitate the transmission and transformation of~~
169 ~~various distributed parameters among component models. MCT coupler exchanges prognostic variables~~
170 ~~from one model to another model component as shown in Figure 1. The WRF model receives sea surface~~
171 ~~temperature (SST) from the ROMS model and supplies the zonal (Uwind) and meridional (Vwind)~~
172 ~~components of 10-m wind, atmospheric pressure (Patm), relative humidity (RH), cloud fraction (Cloud),~~
173 ~~precipitation (Rain), shortwave (Swrad) and longwave (Lwrad) radiation to the ROMS model. The SWAN~~
174 ~~model receives Uwind and Vwind from the WRF model and transfers significant wave height (Hwave) and~~
175 ~~mean wavelength (Lmwave) to the WRF model. A large number of variables are exchanged between~~
176 ~~ROMS and SWAN models. The ocean surface current components (Us, Vs), free surface elevations (η),~~
177 ~~and bathymetry (Bath) provided to the SWAN from ROMS model. The wave parameters i.e. Hwave,~~
178 ~~Lmwave, peak wavelength (Lpwave), wave direction (Dwave), surface wave period (Tpsurf), bottom wave~~
179 ~~period (Tmbott), percentage wave breaking (Ob), wave energy dissipation (DISSwcap), and bottom orbit~~

Formatted: Indent: First line: 1.27 cm

180 velocity (U_{bot}) provided from the SWAN to ROMS model through the MCT coupler. Further details on
181 the COAWST modeling system can be found in Warner et al. (2010).

182

183 2.2 Model configuration and experiment design

184 The coupled model was configured over the BoB to study the ~~VSCS~~-Phailin during the
185 period of ~~10 to 15 October 2013~~ 00 GMT 10 October – 00 GMT 15 October 2013. The setup of
186 COAWST modeling system used in this study included fully coupled atmosphere-ocean-wave
187 (ROMS+WRF+SWAN) models but the sediment transport is not included. A non-hydrostatic,
188 fully compressible atmospheric model with a terrain-following vertical coordinate system, WRF-
189 ARW (version 3.7.1) was used in the COAWST configuration. The WRF model used with 9 km
190 horizontal grid resolution over the domain 65 °E-105 °E, 1°N-34 °N and 30 sigma levels in the vertical.
191 The WRF was initialized with ‘National Centre for Environmental Prediction’ (NCEP) ‘Final Analysis’
192 (FNL) data (NCEPFNL, 2000) at 00 GMT 10 October 2013. The lateral boundary conditions in WRF were
193 provided at 6 hour interval from the FNL data. ~~The atmospheric model We~~ used the parameterization
194 schemes for calculating boundary layer processes, precipitation processes, and surface radiation
195 fluxes. The Monin-Obukhov scheme of surface roughness layer parameterization (Monin and
196 Obukhov 1954) was activated in the model. The Rapid Radiation Transfer Model (RRTM) and
197 cloud-interactive shortwave (SW) radiation scheme from Dudhia (1989) were used. The planetary
198 boundary layer scheme YSU-PBL, described by Noh et al. (2003), was used. At each time step,
199 the calculated value of exchange coefficients and surface fluxes off the land or ocean surface by
200 the atmospheric and land surface layer models (NOAH) passed to the YSU PBL. The Grid-scale
201 precipitation processes were represented by WRF single-moment (WSM) six-class moisture
202 microphysics scheme by Hong and Lim (2006). The sub-grid scale convection and cloud
203 detrainment were taken care by Kain (2004) cumulus scheme.

204 A terrain following ocean model ROMS with 40 sigma levels in the vertical used in this
205 study. The ROMS model domain used with zonal and meridional grid resolutions of 6 km and 4 km,
206 respectively. This high resolution in ROMS enables to resolve mesoscale eddies in the ocean. The vertical
207 starching parameters i.e. θ_s and θ_p were set at 7 and 2, respectively. The northern lateral boundary in ROMS
208 was closed by the Indian subcontinent. The ROMS model observed open lateral boundaries in the west,
209 east, and south in the present configuration. The initial and lateral open boundary conditions were derived

Formatted: Subscript

Formatted: Subscript

210 from the ‘Estimating the Circulation and Climate of the Ocean, Phase II’ (ECCO2) data (Menemenlis et
211 al., 2005). The ocean bathymetry was provided from the 2-minute gridded global relief (ETOPO2) data
212 (National Geophysical Data Center, 2006). There was no relaxation provided to the model for any
213 correction in the temperature, salinity, and current fields. A terrain following ocean model ROMS with
214 40 sigma levels used in this study. The Generic-Length-Scale (GLS) vertical mixing scheme
215 parameterized as the K- ϵ model used (Warner et al., 2005). Tidal boundary conditions were
216 derived from the TPXO.7.2 (<ftp://ftp.oce.orst.edu/dist/tides/Global>) data, which includes phase
217 and amplitude of the M2, S2, N2, K2, K1, O1, P1, MF, MM, M4, MS4, and MN4 tidal constituents
218 along the east coast of India. The tidal input was interpolated from TPXO.7.2 grid to ROMS
219 computational grid. The Shchepetkin boundary condition (Shchepetkin, 2005) for the barotropic
220 current was used at open lateral boundaries of the domain which allowed the free propagation of
221 astronomical tide and wind-generated currents. The domains of atmosphere and ocean models
222 ~~which were part of the COAWST modeling system~~ are shown in Figure 24. ~~The domain for SWAN~~
223 ~~model was similar to the domain of ROMS model.~~ The ROMS and SWAN were configured over
224 the common model domain shown with the shaded bathymetry data in Figure 2. The two locations
225 used for the time series analysis are marked with stars in Figure 2. These two locations, one on-
226 track and another off-track, were selected in the vicinity of the region of maximum surface cooling
227 and wind-stress during the passage of Phailin. The wave model SWAN was forced with the WRF
228 computed wind field. We used 24 frequency (0.04 - 1.0 Hz) and 36 directional bands in SWAN model. The
229 boundary conditions for SWAN were derived from the ‘WaveWatch III’ model. The atmospheric model
230 WRF had 9 km horizontal grid resolution over the domain 65°E-105°E, 1°N-34°N with 30 sigma
231 levels in vertical. WRF was initialized with National Centre for Environmental Prediction (NCEP)
232 Final Analysis (FNL) data (NCEP-FNL, 2000) on 10th October 2013 at 00 GMT. Lateral boundary
233 conditions in WRF provided at 6 h interval from the FNL data. The ROMS model domain had
234 zonal and meridional grid resolutions of 6 km and 4 km, respectively. The northern lateral
235 boundary in ROMS was closed and the model observed open boundaries in rest of the sides. The
236 oceanic initial and lateral open boundary conditions were derived from the Estimating the
237 Circulation and Climate of the Ocean, Phase II (ECCO2) data. Ocean bathymetry was derived
238 from 2 minute gridded global relief data (ETOPO2). In the COAWST system, the free surface
239 elevations (ELV) and current (CUR) simulated by ocean model ROMS are provided to the wave model
240 SWAN. The Kirby and Chen (1998) formulation was used for the computation of currents. The surface
241 wind applied to the SWAN model (provided by WRF) used in the Komen et al. (1984) closure model to

242 transfer energy from the wind to the wave field. The baroclinic time step used in ROMS model was 5 s.
 243 The SWAN and WRF models used with time steps of 120 s and 60 s, respectively. The coupled modeling
 244 system allows the exchange of prognostic variables among the atmosphere, ocean, and wave
 245 models at every 600 s. The SST simulation at high spatial and temporal resolutions enables
 246 accurate heat fluxes at the air-sea interface and exchange of heat between oceanic mixed layer and
 247 atmospheric boundary layer. The surface roughness parameter calculated in the WRF model based
 248 on Taylor and Yelland (2001), which involved parameters from the wave model. ~~The Advanced~~
 249 ~~Very High Resolution Radiometer (AVHRR) data was used for the validation of model simulated~~
 250 ~~SST.~~

251

252 2.3. Methodology

253 The baroclinic current component was calculated by subtracting the barotropic component
 254 from the mean current with a resolution of 2 m in the vertical. The power spectrum analysis was
 255 performed on the zonal and meridional baroclinic currents along the depth section of the selected
 256 locations by using periodogram method (Auger and Flandrin, 1995). The continuous wavelet
 257 transform using Morlet wavelet method (Lilly and Olhede, 2012) carried out to analyze the
 258 temporal variability of the baroclinic current at a particular level of 14 m. The near-inertial
 259 baroclinic velocities were filtered by the Butterworth 2nd order scheme for the cutoff frequency
 260 range ~~of 0.028 to 0.038 cycle hr⁻¹ of 0.033 to 0.043.~~ The filtered zonal (u_f) and meridional (v_f)
 261 inertial baroclinic currents were used to calculate the inertial baroclinic kinetic energy (E_I) in m²
 262 s⁻² and inertial shear (S_I) following Zhang et al. (2014) using equation (1).

263

$$S_f^2 = \left(\frac{\partial u_f}{\partial z}\right)^2 + \left(\frac{\partial v_f}{\partial z}\right)^2 \quad (1)$$

264

265

~~$$S_f = \left(\frac{\partial u_f}{\partial z}\right)^2 + \left(\frac{\partial v_f}{\partial z}\right)^2 \quad (1)$$~~

266 As the stratification is a measure of oceanic stability, the buoyancy frequency (N) was calculated
 267 using equation (2)

Formatted: Not Superscript/ Subscript

268
$$N^2 = -\frac{g}{\rho} \frac{\partial \rho}{\partial z} \quad (2)$$

269 Where ρ is the density of sea-water and g is the acceleration due to gravity.

270 The analysis of generation of the inertial oscillations and their dissipation was performed
271 on the basis of turbulent dissipation rate (ϵ) and turbulent eddy diffusivity (k_ρ). These parameters
272 were calculated by using following formula (Mackinnon and Gregg, 2005; van der Lee and
273 Umlauf, 2011; Palmer et al., 2008; Osborn, 1980)

274
$$\epsilon = \epsilon_0 \left(\frac{N}{N_0} \right) \left(\frac{S_{lf}}{S_0} \right) \quad (3)$$

275
$$k_\rho = 0.2 x \left(\frac{\epsilon}{N^2} \right) \quad (4)$$

276 Where S_{lf} is the low shear background velocity, Values of $N_0 = S_0 = 3$ cycle per hour and $\epsilon_0 =$
277 $10^{-8} \text{ W kg}^{-1}$.

278

279 3. Results and Discussion

280 3.1. Details of VSCS Phailin

281 ~~Phailin, a very severe cyclonic storm (VSCS) was developed over the BoB in northern~~
282 ~~Indian Ocean in October 2013. The landfall of Phailin occurred on 12 October 2013 around 15:30~~
283 ~~GMT near Gopalpur district of Odisha state at the east coast of India. After the 1999 super cyclonic~~
284 ~~event of the Odisha coast, Phailin was the second strongest cyclonic event that made landfall at~~
285 ~~east coast of India (Kumar and Nair, 2015). The low pressure system developed in the north of the~~
286 ~~Andaman Sea on 7th October 2013, which transformed into a depression on 8th October at 12 °N,~~
287 ~~96 °E. This depression got converted to a cyclonic disturbance on 9th October and further~~
288 ~~intensified while moved to east central BoB and opted the maximum wind speed of 200 km h⁻¹ at~~
289 ~~03:00 GMT on 11th October. Finally, landfall occur at 17:00 GMT 12th October. More details on~~
290 ~~the development and propagation of VSCS Phailin can be found in literature (IMD Report, 2013;~~
291 ~~Mandal et al. 2015; Prakash and Pant, 2017).~~

292 3.1.3.2 Validation of coupled model simulations

293 The WRF model simulated track of Phailin was validated against the India Meteorological
294 Department (IMD) reported best-track of the cyclone. A comparison of model simulated track with
295 the IMD track is shown in Figure 32. Solid circles marked on both the tracks represent the 3-hourly
296 positions of the cyclone's center, as identified by the minimum surface pressure. The daily
297 positions of the centre of Phailin are labelled with the date. WRF model in the coupled
298 configuration does a fairly good job in simulating the track, translational speed, and landfall
299 location of Phailin. The positional track error was about 40 km when compared to IMD track of
300 Phailin. The stand-alone WRF model (not shown here) was found to simulate Phailin track almost
301 similar to the WRF in coupled configuration. However, the intensity (surface wind speed) in WRF
302 stand-alone model was higher as compared to the coupled model. Figure 4 shows the comparison
303 of stand-alone WRF and coupled model simulated mean sea level pressure (MSLP), wind speed,
304 and wind direction at a buoy (BD09) location (marked with a blue circle in Figure 3). It can be
305 inferred from the figure that stand-alone WRF simulated larger pressure drop and higher wind
306 speed as compared to buoy measurements. The WRF in coupled model configuration shows better
307 performance in simulating the surface wind speed and pressure during Phailin. The exchange of
308 wave parameters with the WRF model in coupled configuration provides realistic sea surface
309 roughness that resulted in improvement of surface wind speed.

310 The SST simulated by the ROMS model in coupled and stand-alone configurations
311 ~~simulated SST was was~~ validated against the Advanced Very High Resolution Radiometer
312 (AVHRR) satellite data on each day for the period of Phailin passage over the BoB. Figure 53
313 shows that the coupled model captures the SST spatial pattern reasonably well with about -0.5°C
314 bias in northwestern BoB on 13-14 October. This order of bias in SST could be resulted from the
315 errors in initial and boundary conditions provided to the model. ~~simulations are capturing the SST~~
316 ~~features as well as the magnitude of cooling associated with the storm.~~ The maximum cooling of
317 the sea surface observed on 13th October in the northwestern BoB in both, coupled model and
318 observations. This post-cyclone cooling primarily associated with the cyclone-induced upwelling
319 resulting from the surface divergence driven by the Ekman transport. Thus, the coupled model is
320 reproducing dynamical processes and vertical velocities reasonably well. The stand-alone ROMS
321 model forced with the WRF winds in un-coupled mode overestimates the cyclone-induced cooling
322 with -2.2 °C bias in SST on 13-14 October (Figure 5). The stronger surface winds in stand-alone
323 WRF cause the larger cold bias in stand-alone ROMS model.

3.2.3.3. Cyclone-induced mixing

The coupled atmosphere-ocean-wave simulation is an ideal tool to understand air-sea exchange of fluxes and their effects on the oceanic water column. Surface wind sets up currents on the surface as well as initiate mixing in the interior of the upper ocean. In order to examine the strength of mixing due to VSCS-Phailin, the model simulated vertical temperature profile together with the surface wind speed, zonal and meridional components of wind current, and kinetic energy at the on-track and off-track locations a location 18.75°N , 86.66°E are plotted in Figure 64. Comparatively stronger zonal and meridional currents observed at the off-track location than the on-track location on 12 October. The larger kinetic energy available at the off-track location leads to greater mixing resulting into deeper mixed layer on 12 October as compared to the on-track location. The surface wind speed at the on-track location shows a typical temporal variations of a passing cyclone. The wind speed peaks, drops, and attains second peak as the cyclone approaches, crosses over, and depart the location. The surface currents forced by these large variations in wind speed and direction at the on-track location results into comparatively weaker magnitude than the off-shore location.

The thermocline, defined as the depth of maximum temperature gradient, is usually referred to a location dependent isotherm depth (Kessler, 1990; Wang et al, 2000). Over the BoB region, the depth of 23°C isotherm (D23) found to be an appropriate representative depth of the thermocline (Girishkumar et al., 2013). Based on the density criteria, we calculated the oceanic mixed layer depth (MLD) as the depth where density increased by 0.125 kg m^{-3} from its surface value. The inertial mixing introduced by the cyclone play central role in deepening of D23 and MLD on 12th October 2013. The warmer near-surface waters mixed downward when the cyclone crossed over this location. After the passage of cyclone, shoaling of D23 and MLD observed as a consequence of cyclone induced upwelling that entrain colder waters from the thermocline into the mixed layer. The temperature of the upper surface water (25-m -30 m) decreased by 3.5°C from its maximum value of 28°C after the landfall of the cyclone on 12-13th October at the off-shore location (Figure 6g4a). In response to the strong cyclonic winds, the depth of 23°C isotherm (D23) deepening by 40 m (from 50 m to 90 m) was observed during 04-12 GMT on 12 October. At the same time, the mixed layer depth (MLD), denoted by a thick black line in Figure 6g, deepens by about 15 m. On the other hand, the on-track location showed cooling at the surface only for a

354 short time on 13 October and the deepening of D23 and MLD were 20 m and 10 m, respectively.
355 The inertial mixing introduced by the cyclone play central role in deepening of D23 and MLD on
356 12th October 2013. To examine the role of cyclone induced mixing in modulating the thermohaline
357 structure of ~~upper ocean~~upper ocean, we carried out further analysis on the coupled model
358 simulations as discussed in the following sections.

359

360 3.2.1.3.3.1. Kinetic energy distribution

361 During the initial phase of ~~VSCS~~ Phailin, the zonal and meridional currents were primarily
362 westward and southward, respectively (Figures ~~6c, 6d, 6h, and 6i~~, ~~4b, 4e~~). However, on and after
363 12th October when cyclone attains peak intensity and crosses over the location, alternative temporal
364 sequences of westward/eastward ~~movement~~ in zonal current and southward/northward ~~flow~~ in
365 meridional current were noticed in current profiles (Figures ~~6~~, ~~4b, 4e~~). ~~The F~~Frequency of these
366 reversals in zonal and meridional currents are recognized as near-inertial frequency generated from
367 the storm at ~~these locations. is location (18.75°N, 86.66°E)~~. The direction and magnitude of
368 currents represent a variability ~~within 16-24 hr~~ that corresponds to the presence of near-inertial
369 oscillations at time period for the selected locations. ~~The K~~Kinetic energy (KE) of currents at
370 various depths is a proxy of energy available in the water column that becomes conducive ~~for~~to
371 turbulent and inertial mixing. Time series of KE associated with the barotropic and depth-~~averaged~~
372 baroclinic components of current at the two point locations (18.75° N, 86.66° E) areare illustrated
373 in Figure ~~6e (on-track) and 6j (off-track)~~, ~~4d~~. The KE associated with the baroclinic component
374 found to be much higher than the barotropic component of current at the both on-track and off-
375 shore locations. The depth-~~averaged~~ baroclinic and barotropic current components' KE also depict
376 the impinging oscillatory behavior. The peak magnitude of KE in baroclinic and barotropic
377 currents at the off-shore location found to be $1.2 \text{ m}^2 \text{ s}^{-2}$ and $0.3 \times 10^{-2} \text{ m}^2 \text{ s}^{-2}$, respectively on 12th
378 October at 08:00 GMT. Whereas the magnitude of KE in baroclinic and barotropic currents at the
379 on-shore location were smaller than the off-shore location during the peak intensity of cyclone.
380 The peak magnitude of kinetic energy in baroclinic current at the off-track location was more than
381 double to that of on-track location. The comparatively smaller magnitude of KE at the on-shore
382 location could be associated with the rapid variations in wind speed and direction leading to
383 complex interaction between subsurface currents in the central region of the cyclone. It is worth

384 ~~noting that the time of peak KE in baroclinic currents coincide with the deepening of MLD and~~
385 ~~D23. Therefore, the KE generated in NIO is responsible for sub-surface mixing that acts to deepen~~
386 ~~the mixed layer.~~ The analysis suggests that energy available for mixing process in the water column
387 was mostly confined ~~into~~ the baroclinic currents at various depths.

388

389 ~~3.2.2.3.3.2.~~ Primary frequency and depth of mixing

390 The power spectrum analysis was performed on the time series profiles at ~~the two selected~~
391 ~~locations selected point location (18.75 °N, 86.66 °E)~~ to get a distribution of all frequencies
392 operating in the mixing process during the passage of ~~Phailin, eyelone. As found in the previous~~
393 ~~section, the KE associated with baroclinic currents are dominated over the barotropic currents, the~~
394 ~~The~~ power spectrum analysis performed on ~~the~~ zonal and meridional components of ~~the~~ baroclinic
395 current profile ~~and is~~ shown in Figure ~~7~~5. It is clear from ~~the figure Figure 5~~ that ~~the~~ tidal (M2, ~~the~~
396 ~~semidiurnal component of tide~~) and near-inertial oscillations (f) are ~~the~~ two dominant frequencies
397 on the surface during the cyclone Phailin. ~~Further, the near inertial frequency is smaller than the~~
398 ~~tidal frequency on the surface. Under the influence of cyclonic winds, the NIO signal was stronger~~
399 ~~(0.84 m2s-2) at the off-track than the on-track location. The depth penetration of NIO was up to~~
400 ~~50 m and 35 m at the off-track and on-track location, respectively. The tidal frequency (M2) and~~
401 ~~inertial frequency (f) bands shown in the Figure 7 implies that the inertial oscillations were~~
402 ~~dominant over the tidal constituent in zonal and meridional baroclinic currents. To analyze the~~
403 ~~mixing potential of the NIO, power spectrum method was applied at the profile of baroclinic~~
404 ~~current component (Figure 5). At the off-track location, The~~the largest power of the NIO was
405 noticed at 14 m depth but the tidal oscillations were ~~almost~~ absent ~~in the along the whole~~ vertical
406 section of baroclinic current (Figure 7). This finding motivated ~~us~~ to analyze the significance and
407 distribution of ~~these~~this sub-surface variability that resulted ~~into~~ ~~an~~ anomalous deepening of MLD.
408 ~~The~~ Highest power of this signal ~~at the off-track location~~ was associated within 0-15 m with ~~the~~
409 magnitude of 0.84 m² s⁻¹ in zonal baroclinic current and within 0-38 m with ~~the~~ magnitude of 0.76
410 m² s⁻¹ ~~in meridional baroclinic current~~. These signals, however, weaken with increasing depth and
411 almost disappeared around 120 m depth. These NIO ~~were~~ ~~are~~ the strongest signals at the 14 m
412 depth ~~in presence of local wind stress that and dominating dominated~~ the mixing ~~compared to any~~
413 ~~other process by any other process than the local wind stress. Other processes include the~~

414 background flows, the presence of eddies, variations in sea surface height, non-linear wave-wave
415 and wave-current interactions (Guan et al., 2014; Park and Watts, 2005).

416 The second order butterworth filter was applied on the baroclinic current components in
417 order to get the strength of NIO in the frequency range of 0.028 to 0.038 cycles h^{-1} at the selected
418 locations. The filtered baroclinic current was further utilized to calculate the filtered inertial
419 baroclinic KE (E_f in m^2s^{-2}). The daily profiles of baroclinic KE were analysed at the two selected
420 locations and shown in Figure 8. The peak baroclinic KE differs from $0.14 m^2s^{-2}$ at the on-track to
421 $0.23 m^2s^{-2}$ at the off-track location on 12 October. As shown in Figures 6 and 7, the filtered
422 baroclinic KE profiles (Figure 8) confirm the dominant presence of NIO at the off-track location
423 as compared to the on-track location. The decay of NIO with the increasing depth was noticed at
424 both the locations. However, the NIO baroclinic KE penetrated up to 80 m in case of off-track as
425 compared to only 50 m at the on-track location. The analysis, therefore, suggests that the NIO
426 generated during the Phailin were more energetic at the selected off-track location, which was also
427 the location of maximum surface cooling as noticed in Figure 5. Therefore, the further analysis in
428 the subsequent sections is limited to the off-track location only. In order to analyze the time
429 distribution of the strong NIO, wavelet transform analysis was applied on the zonal and meridional
430 baroclinic currents at 14 m depth. The Scalogram, shown in Figure 96, depicts the generation of
431 NIO signal at the off-track location on 12th October that subsequently got strengthen and attains
432 its peak value on the mid of 13th October. The energy percentage of the meridional component was
433 always lower than the zonal component. The peak values of energy percentage was found in the
434 time periods between 1-1.3 days, 25-28 hr marked with a white dashed line in Figure 6. A
435 Butterworth 2nd-order band pass filter was applied at the corresponding cutoff frequency interval
436 of 0.033–0.043 to filter the NIO signal of the baroclinic zonal and meridional current. Figure 7
437 shows profiles of near inertial zonal (U_i) and meridional (V_i) baroclinic current together with the
438 kinetic energy (E_i) of near inertial flow. The maximum strength of inertial baroclinic current was
439 $0.3 m s^{-1}$ with the signature of an alternate directional reversal of current signals. Presence of these
440 inertial currents were up to 70 m depth with peak value of kinetic energy E_i being $0.048 m^2 s^{-2}$. It
441 can be noticed from Figure 7c, the baroclinic kinetic energy remains higher ($> 0.03 m^2 s^{-2}$) only
442 from mid of 11th October till the end of 12th October and thereafter the energy rapidly decreases
443 and almost disappeared after 13th October. This indicates the period of prominent mixing due to

Formatted: Superscript

Formatted: Subscript

Formatted: Superscript

Formatted: Superscript

Formatted: Superscript

Formatted: Superscript

Formatted: Superscript

Formatted: Superscript

444 NIO was 11–12 October 2013. The daily averaged values of baroclinic kinetic energy (not shown
445 here) also confirms the maxima in E_T on 11–12 October with the vertical extent up to 80 m depth.

446 3.2.3.3.3. Role of downward propagation of energy

447 To investigate the energy propagation from the surface to the interior layers of upper-
448 ocean, we derived the rotary spectra (Gonella, 1972; Hayashi, 1979) of near-inertial wave numbers
449 and shown in Figure 10-8. The daily averaged vertical wave-number rotary spectra provides a clear
450 picture of wind energy distribution in the sub-surface water. The anticyclonic spectrum (A_m) is
451 dominating over the cyclonic spectra (C_m) for the entire duration of the cyclone. This feature
452 indicates that the energy is propagating downward generated by these inertial oscillations. The
453 Mmagnitude of these oscillations increased from initial stage up to 12th October and remained at
454 high energy density for the rest of the cyclone period. This downward directed energy initiated a
455 process of mixing between the mixed layer and the thermocline. This energy helps to deepen the
456 mixed layer against oceanic stratification by introducing a strong shear. The buoyancy of stratified
457 ocean was overcome to some extent by the shear generated that assist in mixing process during the
458 very severe cyclone. ~~For the current case, kinetic energy (Figure 7e) represents the analogical~~
459 ~~behavior as reported by Alford and Gregg (2001). Their study Alford and Gregg (2001) highlighted~~
460 ~~that, in most of the cases, the energy of inertial oscillations potentially penetrates the mixed layer~~
461 ~~but suddenly drops down as it touches the thermocline. The energy dissipation mechanism studied~~
462 ~~in few other studies (Chant, 2001; Jacob, 2003).~~

463 The 2-layer model described by Burchard and Rippeth (2009) illustrated the process of
464 generation of sufficient shear to start mixing near the thermocline. Their simple model ignored the
465 effect of the lateral density gradient, mixing, and advection. Burchard et al. (2009) mentioned four
466 important parameters for the shear generation, i.e. surface wind stress ($P_s S^2$), bed stress ($-D_b S^2$),
467 interfacial stress ($-D_i S^2$), and barotropic flow ($P_m S^2$). Utilizing simulations from our coupled
468 atmosphere-ocean-wave model, we calculated individual terms as suggested by Burchard et al.
469 (2009) and presented in Figure 9-10. ~~It is clear from the figure that the surface wind stress term~~
470 ~~plays most significant role~~ Surface wind stress found to be the most dominating term in modulating
471 the magnitude of bulk shear during the stormy event. ~~Rest of the terms were~~ Other terms were
472 ~~found to be~~ relatively weaker and, therefore, contributing only marginally ~~in to~~ the variability of
473 the bulk shear.

Formatted: Subscript

Formatted: Subscript

474 To examine the generation and dissipation of these inertial ~~oscillations,waves,~~ the shear
475 generated by the near-inertial baroclinic current (S^2) and turbulent kinetic energy dissipation rate
476 (ϵ) were calculated and analyzed. The shear produced by inertial oscillations ~~was increasing~~
477 ~~increased at 20-80 m depth from 40-80 m depth~~ and higher magnitude was associated with peak
478 wind speed of cyclone (Figure ~~40a~~12a). This shear overcome the stratification (Figure ~~40b~~12b),
479 ~~represented by buoyancy frequency N^2 ,~~ and played important role in mixing and deepening of the
480 ~~thermocline and mixed layer on 12th October, that was weak at this depth compared to the shear~~
481 ~~of the near inertial waves.~~ The value of kinetic energy dissipation rate (ϵ) increased from 4×10^{14}
482 to $2.5 \times 10^{-13} \text{ W kg}^{-1}$ on approaching the thermocline (Figure ~~40e~~12c). The increase in ϵ indicates
483 ~~the~~ weakening of the shear generated by the inertial waves leading to ~~the~~ fast disappearance of
484 these baroclinic instabilities from the region. ~~The non-linear interaction between the NIO and~~
485 ~~internal tides together with the prevailing background currents cause rapid dissipation of kinetic~~
486 ~~energy in the thermocline. Guan et al. (2014) also reported an accelerated dampening of NIO~~
487 ~~associated with the wave-wave interactions between NIO and internal tides. The background~~
488 ~~currents found to modify the propagation of NIO (Park and Watts, 2005).~~ The magnitude of the
489 turbulent eddy diffusivity (K_ρ), shown in Figure ~~40d~~12d, implies that the greater mixing takes
490 place within the mixed layer ~~place~~ where K_ρ -was high (6.3×10^{-11} to $1.2 \times 10^{-11} \text{ m}^2 \text{ s}^{-1}$). The daily
491 averaged values of ϵ and K_ρ were $1.2 \times 10^{-13} \text{ W kg}^{-1}$ and $1.5 \times 10^{-10} \text{ m}^2 \text{ s}^{-1}$, respectively on 12th
492 October, which were higher as compared to the initial two days of the cyclonic event. ~~Therefore,~~
493 ~~Results from the present study,~~ as well as the conclusions from the past studies, indicate that
494 wave-current interaction, mesoscale processes, and wave-wave interaction can affect the process
495 of downward mixing and cause the dissipation of inertial oscillations.

496 4. Conclusions

497 Processes controlling the sub-surface mixing were evaluated under the high wind speed
498 regime of a severe cyclonic storm Phailin over the BoB. A coupled atmosphere-ocean-wave
499 (WRF+ROMS+SWAN) model as part of the COAWST modeling system was used to simulate
500 atmospheric and oceanic conditions during the passage of Phailin cyclone. A detailed analysis of
501 model simulated data revealed interesting features of generation, propagation, and dissipation of
502 kinetic energy in the upper oceanic water column. Deepening of the MLD and thermocline by 15
503 m and 40 m, respectively were explained through the strong shear generated by the inertial

Formatted: Superscript

Formatted: Superscript

504 oscillations that helped to overcome the stratification and initiate mixing at the base of the mixed
505 layer. However, there was a rapid dissipation of the shear with increasing depth below the
506 thermocline. The peak magnitude of kinetic energy in baroclinic and barotropic currents found to
507 be $1.2 \text{ m}^2 \text{ s}^{-2}$ and $0.3 \times 10^{-2} \text{ m}^2 \text{ s}^{-2}$, respectively. The power spectrum analysis suggested a dominant
508 frequency operative in sub-surface mixing that was associated with near-inertial oscillations. The
509 peak strength of $0.84 \text{ m}^2 \text{ s}^{-1}$ in the zonal baroclinic current found at 14 m depth at a location in
510 northwestern BoB. The baroclinic kinetic energy remains higher ($> 0.03 \text{ m}^2 \text{ s}^{-2}$) during 11-12
511 October and decreased rapidly thereafter. The wave-number rotary spectra identified the
512 downward propagation, from the surface up to the thermocline, of energy generated by inertial
513 oscillations. A quantitative analysis of shear generated by the near-inertial baroclinic current
514 showed higher shear generation at 20-80 m depth during peak surface winds. Analysis highlights
515 that greater mixing within the mixed layer takes place where the eddy kinetic diffusivity was high
516 ($> 6 \times 10^{-11} \text{ m}^2 \text{ s}^{-1}$). The turbulent kinetic energy dissipation rate increased from 4×10^{-14} to $2.5 \times 10^{-$
517 13 W kg^{-1} on approaching the thermocline that dampened mixing process further down into the
518 thermocline layer. Kinetic energy associated with baroclinic currents were about two order of
519 magnitudes higher than in barotropic component. The peak strength of $0.84 \text{ m}^2 \text{ s}^{-1}$ in zonal
520 baroclinic current was found at 14 m depth at a location in northwestern BoB. The wave-current
521 interaction, mesoscale processes, and wave-wave interaction increased the dissipation rate of shear
522 and, thereby, limited the downward mixing up to the thermocline. were found to affect the process
523 of downward mixing and cause the dissipation of inertial oscillations. The coupled model found
524 to be a useful tool to investigate air-sea interaction, kinetic energy propagation, and mixing in the
525 upper-ocean and oceanic sub-surface processes. The results from this study highlight the
526 importance of atmosphere-ocean coupling for better understanding of oceanic response under the
527 strong wind conditions. The proper representation of kinetic energy propagation and oceanic
528 mixing have applications in improving the intensity prediction of cyclone, storm surge forecasting,
529 and biological productivity.

530

531 **Author contribution:** KRP and TN performed model simulations and analyzed data. VP prepared
532 the manuscript with contributions from all co-authors.

533 **Acknowledgements**

534 ECCO2 is a contribution to the NASA Modeling, Analysis, and Prediction (MAP)
535 program. The study benefitted from the funding support from Ministry of Earth Sciences, Govt. of
536 India and Space Applications Centre, Indian Space Research Organisation. High Performance
537 Computing (HPC) facility provided by IIT Delhi and Department of Science and Technology
538 (DST), Govt. of India are thankfully acknowledged. Authors are thankful to Dr. Lingling Xie for
539 his productive suggestions. Graphics generated in this manuscript using Ferret and NCL. TN and
540 KRP acknowledge MoES and UGC-CSIR, respectively for their doctoral fellowship support.

541

542

543

544

545

546

547

548

549

550

551

552

553 **References**

554 Alam, M. M., Hossain, M.A. and Shafee, S.: Frequency of Bay of Bengal cyclonic storms and
555 depressions crossing different coastal zones, *Int. J. Climatol.*, 23, 1119–1125,
556 doi:10.1002/joc.927, 2003.

557 Alford, M.H., Gregg, M.C.: Near-inertial mixing: modulation of shear, strain and microstructure
558 at low latitude. *J. Geophys. Res.* 106 (C8), 16947–16968, 2001.

559 [Auger F., Flandrin, P.: Improving the Readability of Time-Frequency and Time-Scale](#)
560 [Representations by the Reassignment Method. IEEE Transactions on Signal Processing. 43,](#)
561 [1068–1089, 1995.](#)

562 Booi, N., Ris, R. C., and Holthuijsen, L. H.: A third-generation wave model for coastal regions,
563 Part I, Model description and validation, J. Geophys. Res., 104(C4), 7649–7666,
564 doi:10.1029/98JC02622, 1999.

565 Burchard, H., Rippeth, T.P.: Generation of bulk shear spikes in shallow stratified tidal seas. J.
566 Phys. Oceanogr. 39, 969–985, 2009.

567 ~~[Chang, J., Chung, C. C., Gong, G. C.: Influences of cyclones on chlorophyll a concentration and](#)~~
568 ~~[Synechococcus abundance in a subtropical western Pacific coastal ecosystem. Mar. Ecol. Prog-](#)~~
569 ~~[Ser. 140, 199–205, 2008.](#)~~

570 Chang, S. W., and Anthes, F.A.: The mutual response of the tropical cyclone and the ocean. J.
571 Phys. Oceanogr., 9, 128–135, 1979.

572 Chant, R.J.: Evolution of near-inertial waves during an upwelling event on the New Jersey Inner
573 Shelf. J. Phys. Oceanogr. 31, 746–764, 2001.

574 [Chen, S., Chen, D., Xing, J.: A study on some basic features of inertial oscillations and near-inertial](#)
575 [internal waves. Ocean Science, 13 \(5\), 829-836, 2017.](#)

576 Chassignet, E.P., Arango, H.G., Dietrich, D., Ezer, T., Ghil, M., Haidvogel, D.B., Ma, C.C.,
577 Mehra, A., Paiva, A.M., Sirkes, Z.: DAMEE-NAB: the base experiments. Dyn. Atmos. Oceans
578 32, 155–183, 2000.

579 Cione, J. J., and Uhlhorn, E.W.: Sea surface temperature variability in hurricanes: Implications
580 with respect to intensity change, Mon. Weather Rev., 131, 1783–1796, doi:10.1175//2562.1,
581 2003.

582 Dudhia, J.: Numerical study of convection observed during the winter —monsoon experiment
583 using a mesoscale two dimensional model. J Atmos Sci, 46, 3077–3107, 1989.

584 Gill, A. E.: On the behavior of internal waves in the wake of storms, J. Phys. Oceanogr., 14, 1129
585 – 1151, 1984.

586 [Girishkumar, M. S., Ravichandran, M., Han, W.: Observed intraseasonal thermocline variability](#)
587 [in the Bay of Bengal. *J. Geophys. Res. Oceans*, 118, 3336–3349, doi:10.1002/jgrc.20245, 2013.](#)

588 Gonella, J.: A study of inertial oscillations in the upper layers of the oceans. *Deep-Sea Res.*, 18,
589 775–788, 1971.

590 [Gonella, J.: A rotary-component method for analysing meteorological and oceanographic vector](#)
591 [time series. *Deep-Sea Research* 19, 833–846, 1972.](#)

592 [Guan, S., Zhao, W., Huthnance, J. Tian, J., and Wang, J.: Observed upper ocean response to](#)
593 [typhoon Megi \(2010\) in the Northern South China Sea. *J. Geophys. Res. Oceans*, 119, 3134–](#)
594 [3157, doi:10.1002/2013JC009661, 2014.](#)

595 Haidvogel, D.B., Arango, H.G., Budgell, W.P., Cornuelle, B.D., Curchitser, E., Di Lorenzo, E.,
596 Fennel, K., Geyer, W.R., Hermann, A.J., Lanerolle, L., Levin, J., McWilliams, J.C., Miller,
597 A.J., Moore, A.M., Powell, T.M., Shchepetkin, A.F., Sherwood, C.R., Signell, R.P., Warner,
598 J.C., Wilkin, J.: Regional ocean forecasting in terrain-following coordinates: model formulation
599 and skill assessment. *Journal of Computational Physics* 227, 3595–3624, 2008.

600 Haidvogel, D.B., Arango, H.G., Hedstrom, K., Beckmann, A., Malanotte-Rizzoli, P.
601 Shchepetkin, A.F.: Model evaluation experiments in the North Atlantic Basin: Simulations in
602 nonlinear terrain-following coordinates. *Dyn Atmos Oceans* 32, 239–281, 2000.

603 [Hayashi, Y.: Space-time spectral analysis of rotary vector series. *J. Atmos. Sci.* 36 \(5\), 757–766,](#)
604 [1979.](#)

605 Hong, S.Y., Lim, J.O.J.: The WRF single-moment 6-class microphysics scheme (WSM6). *J*
606 *Korean Meteor Soc* 42:2, 129-151, 2006.

607 IMD Report.: Very Severe Cyclonic Storm, PHAILIN over the Bay of Bengal (08-14 October
608 2013) A Report. India Meteorological Department, Technical Report, October 2013.

609 Jacob, S.D., Shay, L.K.: The role of oceanic mesoscale features on the tropical cyclone-induced
610 mixed layer response: A case study. *J. Phys. Oceanog.*, 33, 649- 676, 2003.

611 Jacob, R., Larson, J., Ong, E.: M x N Communication and Parallel Interpolation in CCSM Using
612 the Model Coupling Toolkit. Preprint ANL/MCSP1225-0205. Mathematics and Computer
613 Science Division, Argonne National Laboratory, 25 pp, 2005.

614 Johnston, T.M.S., Chaudhuri, D., Mathur, M., Rudnick, D.L., Sengupta, D., Simmons, H.L.,
615 Tandon, A., and Venkatesan, R.: Decay mechanisms of near-inertial mixed layer oscillations in
616 the Bay of Bengal, *Oceanography*, 29(2): 180–191, doi:10.5670/oceanog.2016.50, 2016.

~~617 Kirby, J. T., and Chen T.M.: Surface waves on vertically sheared flows: Approximate
618 dispersion relations, *J. Geophys. Res.*, 94(C1),1013–1027, doi:10.1029/JC094iC01p01013,
619 1989.~~

620 Kain, J.S.: The Kain-Fritsch convective parameterization: An update. *J Appl Meteor* 43, 170–
621 181, 2004.

622 Kessler, W. S.: Observations of long Rossby waves in the northern tropical Pacific. *J. Geophys.*
623 *Res.*, 95, 5183–5217, 1990.

~~624 Kirby, J. T., and Chen T.M.: Surface waves on vertically sheared flows: Approximate
625 dispersion relations, *J. Geophys. Res.*, 94(C1),1013–1027, doi:10.1029/JC094iC01p01013,
626 1989. 1989.~~

627 Komen, G.J., Hasselmann, S., and Hasselmann, K.: On the existence of a fully developed wind-
628 sea spectrum. *J. Phys. Oceanogr.*, 14, 1271–1285. 1984.

629 Kumar VS, Nair A.M.: Inter-annual variations in wave spectral characteristics at a location off the
630 central west coast of India. *Ann Geophys* 33:159–167, doi:10.5194/angeo-33-159, 2015.

~~631 Latha, T.P., Rao, K.H., Nagamani, P.V., Amminedu, E., Choudhury, S.B., Dutt, C.B.S., and
632 Dadhwal, V.K.: Impact of Cyclone PHAILIN on chlorophyll a concentration and productivity
633 in the Bay of Bengal. *International Journal of Geosciences* 6:473–480,
634 doi:10.4236/ijg.2015.65037, 2015.~~

635 Leipper, D. F.: Observed Ocean Conditions and Hurricane Hilda, 1964, *J. Atmos. Sci.*, 24, 182–
636 186, doi:10.1175/1520-0469(1967)0242.0.CO;2, 1967.

637 Zhi, Li., Yu, W., Li, T., Murty, V.S.N., and Tangang, F.: Bimodal character of cyclone
638 climatology in the Bay of Bengal modulated by monsoon seasonal cycle. *J Climate* 26:1033-
639 1046. doi: 10.1175/JCLI-D-11-00627.1, 2013.

640 ~~Lin, I.I., Liu, W.T., Wu, C.C., Wong, T.F., Hu, C., Chen, Z., Liang, W.D., Yang, Y., Liu, K.K.:~~
641 ~~New evidence for enhanced ocean primary production triggered by tropical cyclone. *Geophys.*~~
642 ~~*Res. Lett.* 30 (13), doi:10.1029/2003GL017141, 2003.~~

643 ~~Lin, I.I., Wu, C.C., Pun, I.F., Ko, D.S.: Upper ocean thermal structure and the western North~~
644 ~~Pacific category 5 typhoons. Part I: ocean features and category 5 typhoon's intensification.~~
645 ~~*Mon. Weather Rev.* 136, 3288–3306, 2008.~~

646 Lilly, J. M., Olhede, S. C.: Generalized Morse Wavelets as a Superfamily of Analytic Wavelets.
647 *IEEE Transactions on Signal Processing.* 60 (11), 6036–6041, 2012.

648 Longshore, D.: *Encyclopedia of Hurricanes, Typhoons, and Cyclones*, 468 pp., Checkmark, New
649 York, 2008.

650 Larson, J., Jacob, R., Ong, E.: *The Model Coupling Toolkit: A New Fortran90 Toolkit for*
651 *Building Multiphysics Parallel Coupled Models.* Preprint ANL/MCS- P1208-1204.
652 Mathematics and Computer Science Division, Argonne National Laboratory, 25 pp, 2004.

653 Lukas, R., and Lindstrom, E.: The mixed layer of the western equatorial Pacific Ocean, *J. Geophys.*
654 *Res.*, 96, 3343–3357, 1991.

655 ~~MacKinnon, J.A., Gregg, M.C.: Mixing on the late summer New England Shelf—solibores, shear~~
656 ~~and stratification. *J. Phys. Oceanogr.* 33 (7), 1476–1492, 2003.~~

657 MacKinnon, J.A., Gregg, M.C.: Spring Mixing: Turbulence and Internal Waves during
658 Restratification on the New England Shelf. *Journal of Physical Oceanography.* 35:12, 2425-
659 2443 2005.

660 Mandal M., Singh K. S., Balaji M., Mohapatra M.: Performance of WRF-ARW model in real-
661 time prediction of Bay of Bengal cyclone ‘Phailin’. *Pure Appl. Geophys* DOI 10.1007/s00024-
662 015-1206-7, 2015.

663 [Menemenlis, D., et al., NASA supercomputer improves prospects for ocean climate research, Eos](#)
664 [Trans. AGU, 86\(9\), 89–96, doi:10.1029/2005EO090002, 2005.](#)

665 Monin, A.S., Obukhov, A.M.F.: Basic laws of turbulent mixing in the surface layer of the
666 atmosphere. *Contrib Geophys Inst Acad Sci USSR 151*:163, e187, 1954.

667 National Centers for Environmental Prediction/National Weather Service/NOAA/U.S.
668 Department of Commerce: NCEP FNL Operational Model Global Tropospheric Analyses,
669 continuing from July 1999. Research Data Archive at the National Center for Atmospheric
670 Research, Computational and Information Systems Laboratory. Dataset.
671 <https://doi.org/10.5065/D6M043C6>, 2000.

672 [National Geophysical Data Center. 2-minute Gridded Global Relief Data \(ETOPO2\) v2. National](#)
673 [Geophysical Data Center, NOAA. doi:10.7289/V5J1012Q, 2006.](#)

674 Neetu, S., Lengaigne, M., Vincent, E.M., Vialard, J., Madec, G., Samson, G., Ramesh Kumar,
675 M.R., and Durand, F.: Influence of upper-ocean stratification on tropical cyclone-induced
676 surface cooling in the Bay of Bengal, *J. Geophys. Res.*, 117, C12020,
677 doi:10.1029/2012JC008433, 2012.

678 Noh, Y., Cheon, W.G., Hong, S.Y., Raasch, S.: Improvement of the K-profile model for the
679 planetary boundary layer based on large eddy simulation data. *Bound Layer Meteor* 107, 401–
680 427, 2003.

681 Osborn, T.R.: Estimates of the Local-Rate of Vertical Diffusion from Dissipation Measurements.
682 *J. Phys. Oceanogr.* 10, 83–89, 1980.

683 Palmer, M.R., Rippeth, T.P., Simpson, J. H.: An investigation of internal mixing in a seasonally
684 stratified shelf sea. *J. Geophys. Res.* 113, C12005, doi:10.1029/2007JC004531, 2008.

685 Pant V, Girishkumar M.S., Udaya Bhaskar T.V.S., Ravichandran M., Papa F., Thangaprakash
686 V.P.: Observed interannual variability of near-surface salinity in the Bay of Bengal, *J. Geophys.*
687 *Res* 120(5):3315–3329, 2015.

688 [Park, J.H., and Watts, D. R.: Near-inertial oscillations interacting with mesoscale circulation in the](#)
689 [southwestern Japan/East Sea. *Geophys. Res. Lett.*, 32, L10611, doi: 10.1029/2005GL022936,](#)
690 [2005.](#)

691 Prakash K.R., Vimlesh Pant: Upper oceanic response to tropical cyclone Phailin in the Bay of
692 Bengal using a coupled atmosphere-ocean model, *Ocean Dynamics*, 67, 51-64,
693 doi:10.1007/s10236-016-1020-5, 2017.

694 Price, J. F., Mooers, C.N., and Van Leer, J.C.: Observation and simulation of storm-induced
695 mixed-layer deepening. *J. Phys. Oceanogr.*, 8, 582-599, [https://doi.org/10.1175/1520-](https://doi.org/10.1175/1520-0485(1978)008<0582:OASOSI>2.0.CO;2)
696 [0485\(1978\)008<0582:OASOSI>2.0.CO;2](https://doi.org/10.1175/1520-0485(1978)008<0582:OASOSI>2.0.CO;2), 1978.

697 Price, J.F.: Upper ocean response to a hurricane. *J. Phys. Oceanogr.*, 11, 153-175, 1981.

698 Rao, R. R., and Sivakumar, R.: Seasonal variability of sea surface salinity and salt budget of the
699 mixed layer of the north Indian Ocean, *J. Geophys. Res.*, 108(C1), 3009,
700 doi:10.1029/2001JC000907, 2003.

701 Sanford, T. B., Black, P.G., Haustein, J., Feeney, J.W., Forristall, G.Z., and Price, J.F.: Ocean
702 response to a hurricane. Part I: Observations. *J. Phys. Oceanogr.*, 17, 2065–2083, 1987.

703 ~~Sarangi, R. K.: Remote sensing based estimation of surface nitrate and its variability in the~~
704 ~~southern peninsular Indian waters, *Int. J. Oceanogr.*, doi:10.1155/2011/172731, 2011.~~

705 ~~Shang, S., Li, L., Sun, F., Wu, J., Hu, C., Chen, D., Ning, X., Qiu, Y., Zhang, C., and Shang, S.,~~
706 ~~Changes of temperature and bio optical properties in the South China Sea in response to~~
707 ~~Typhoon Lingling, (2001), *Geophys. Res. Lett.*, 35, L10602, doi:10.1029/2008GL033502,~~
708 ~~2008.~~

709 ~~Schahinger, R.B.: Near inertial motion on the south Australian shelf. *J. Phys. Oceanogr.*, 18(3),~~
710 ~~492-504, 1988.~~

711 Shchepetkin and A. F., McWilliams J. C.: The Regional Ocean Modeling System: A split-explicit,
712 free-surface, topography following coordinates ocean model, *Ocean Modelling*, 9, 347-404,
713 2005.

714 Skamarock, W.C., Klemp, J.B., Dudhia, J., Gill, D.O., Barker, D.M., Wang, W., —Powers, J.G.:
715 A Description of the Advanced Research WRF Version 2. NCAR Technical Note, NCAR/TN-
716 468+STR., 2005.

717 Shay, L. K., Black, P., Mariano, A., Hawkins, J., and Elsberry, R.: Upper ocean response to
718 hurricane Gilbert, *J. Geophys. Res.*, 97(20), 227–248, 1992.

- 719 Shay, L. K. and Elsberry, R.L.: Vertical structure of the ocean current response to a hurricane. J.
720 Phys. Oceanogr., 19, 649-669, 1989.
- 721 Shay, L. K., Goni, G.J., and Black, P.G.: Effects of a warm oceanic feature on Hurricane Opal,
722 Mon. Weather Rev., 128, 1366–1383, doi:10.1175/1520-0493(2000)128:2.0.CO;2, 2000.
- 723 Shearman, R.K.: Observations of near-inertial current variability on the New England shelf. J.
724 Geophys. Res. 110, C02012, doi:10.1029/2004JC002341, 2005.
- 725 Srinivas, C. V., Mohan, G. M., Naidu, C. V., Baskaran, R., Venkatraman B. :Impact of air-sea
726 coupling on the simulation of tropical cyclones in the North Indian Ocean using a simple 3-D
727 ocean model coupled to ARW. J. Geophys. Res. Atmos., 121, 9400-9421,
728 doi:10.1002/2015JD024431, 2016.
- 729 Suzana, J Carmargo, Adam H Sobel, Anthony G Barnston and Kerry A. Emanuel: Tropical
730 cyclone genesis potential index in climate models. Tellus 59A:428-443, 2007.
- 731 Taylor, P.K., Yelland, M.J.: The dependence of sea surface roughness on the height and steepness
732 of the waves. J. Phys. Oceanogr., 31, 572–590, 2001.
- 733
- 734 Thadathil, P., Muraleedharan, P.M., Rao, R.R., Somayajulu, Y.K., Reddy, G.V., and
735 Revichandran, C.: Observed seasonal variability of barrier layer in the Bay of Bengal, J.
736 Geophys. Res., 112, C02009, doi:10.1029/2006JC003651, 2007.
- 737 Varkey, M. J., Murty, V.S.N., and Suryanarayana, A.: Physical oceanography of the Bay of Bengal
738 and Andaman Sea, Oceanogr. Mar. Biol., 34, 1–70, 1996.
- 739 van der Lee, E.M., and Umlauf, L.: Internal wave mixing in the Baltic Sea: near-inertial waves in
740 the absence of tides. J. Geophys. Res. 116, C10016, doi:10.1029/2011JC007072, 2011.
- 741 Vinayachandran, P. N., Murty, V.S.N., and Ramesh Babu V.: Observations of barrier layer
742 formation in the Bay of Bengal during summer monsoon, J. Geophys. Res., 107(C12), 8018,
743 doi:10.1029/2001JC000831, 2002.
- 744 Vissa, N.K., Satyanarayana, A.N.V. and Prasad Kumar, B.: Intensity of tropical cyclones during
745 pre- and post-monsoon seasons in relation to accumulated tropical cyclone heat potential over
746 Bay of Bengal, Nat Hazards 68: 351. <https://doi.org/10.1007/s11069-013-0625-y>. 2013.

Formatted: Justified, Indent: Left: 0 cm, Hanging: 0.5 cm

747 [Wang, B., Wu, R., and Lukas R.: Annual adjustment of the thermocline in the tropical Pacific](#)
748 [Ocean, J. Clim., 13, 596–616, 2000.](#)

749 Warner, J. C., Sherwood, C.R., Arango, H.G., and Signell, R.P.: Performance of four turbulence
750 closure models implemented using a generic length scale method, *Ocean Modell.*, 8, 81–113,
751 doi:10.1016/j. oцемod.2003.12.003, 2005.

752 Warner, J.C., Armstrong B., He R., Zambon J.B.: Development of a coupled ocean–
753 atmosphere–wave–sediment transport (COAWST) modeling system. *Ocean modelling* 35:230–
754 244. doi:10.1016/j. oceanmod.2010.07.010, 2010.

755 Yanase, W., Satosh, M., Taniguchi, H., and Fujinami, H.: Seasonal and Intraseasonal Modulation
756 of tropical cyclogenesis environment over the Bay of Bengal during the extended summer
757 monsoon. *J Climate* 25:2914-2930. doi: 10.1175/JCLI-D-11-00208.1, 2012.

758 Zhang, S., Xie, L., Hou, Y., Zhao, H., Qi, Y., & Yi, X.: Tropical storm-induced turbulent mixing
759 and chlorophyll-a enhancement in the continental shelf southeast of Hainan Island. *Journal of*
760 *Marine Systems*, 129, 405-414, 2014.

761 ~~[Zhao, H., Tang, D.L., Wang, D.X.: Phytoplankton blooms near the Pearl River Estuary induced](#)~~
762 ~~[by Typhoon Nuri. J. Geophys. Res. 114, C12027, doi:10.1029/2009JC005384, 2009.](#)~~

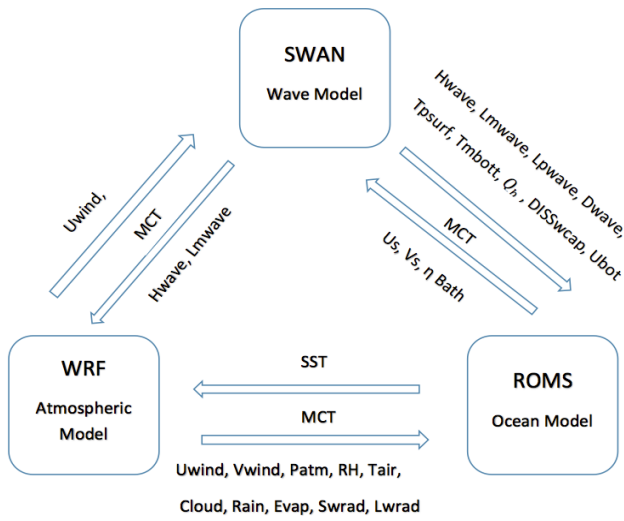
763

764

765

766

767



768

769 **Figure 1:-The block diagram showing the component models WRF, ROMS, and SWAN of the**
 770 **COAWST modeling system together with the variables exchanged among the models. MCT- the**
 771 **model coupling toolkit is a model coupler used in the COAWST system.**

772

773

774

775

776

777

778

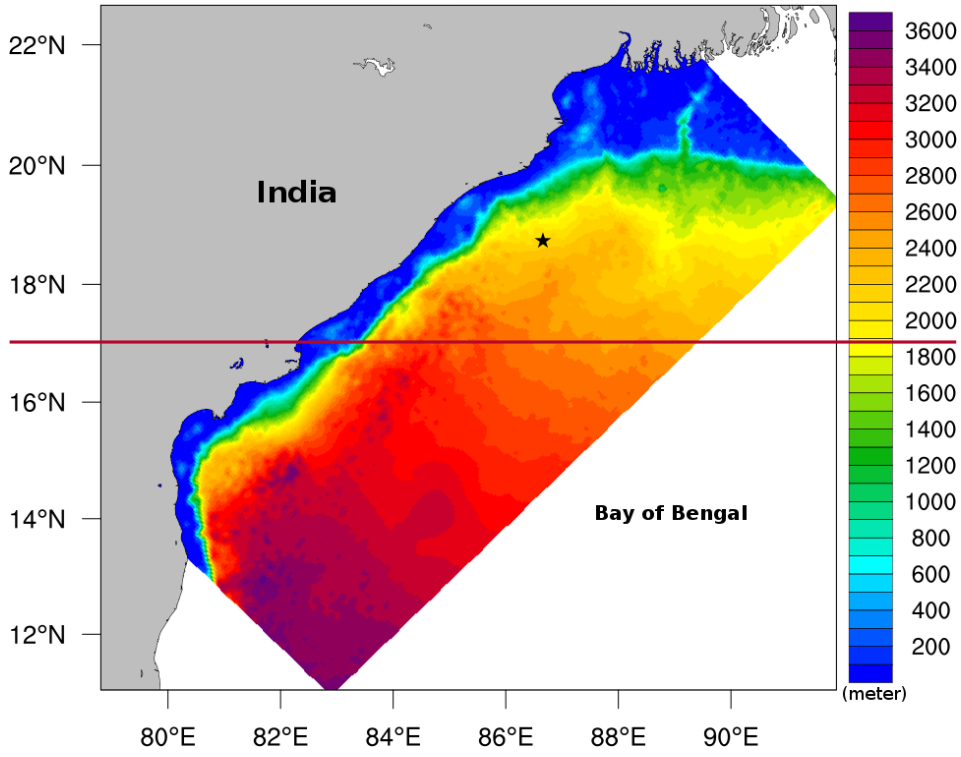
779

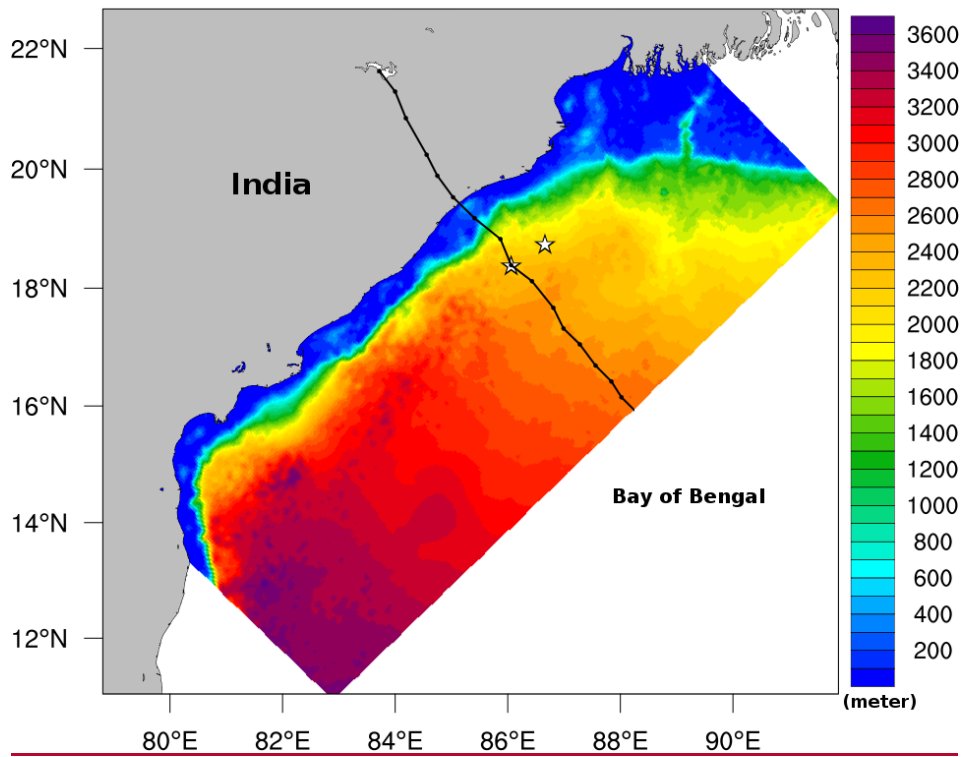
780

781

782

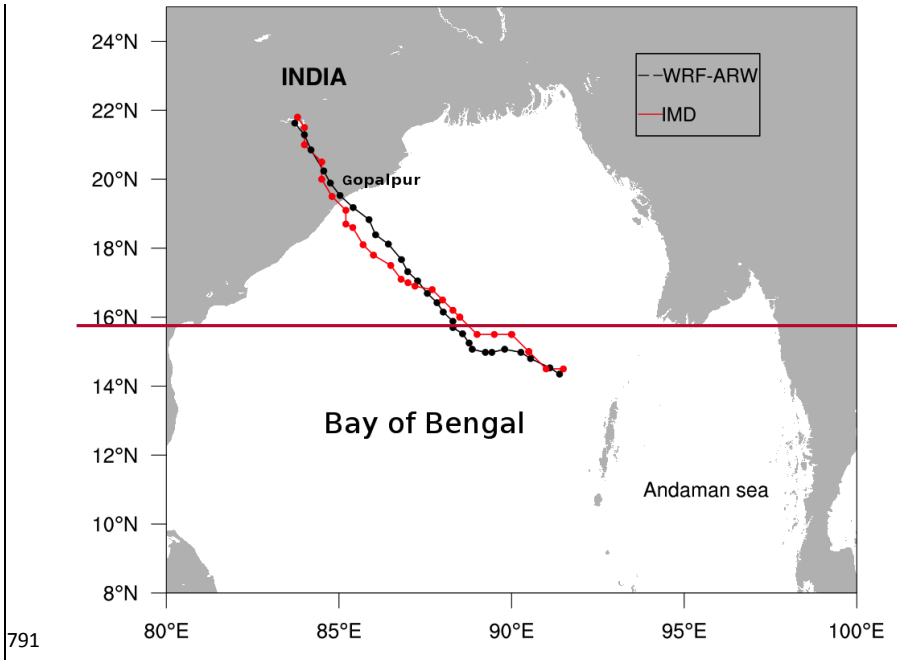
Formatted: Justified



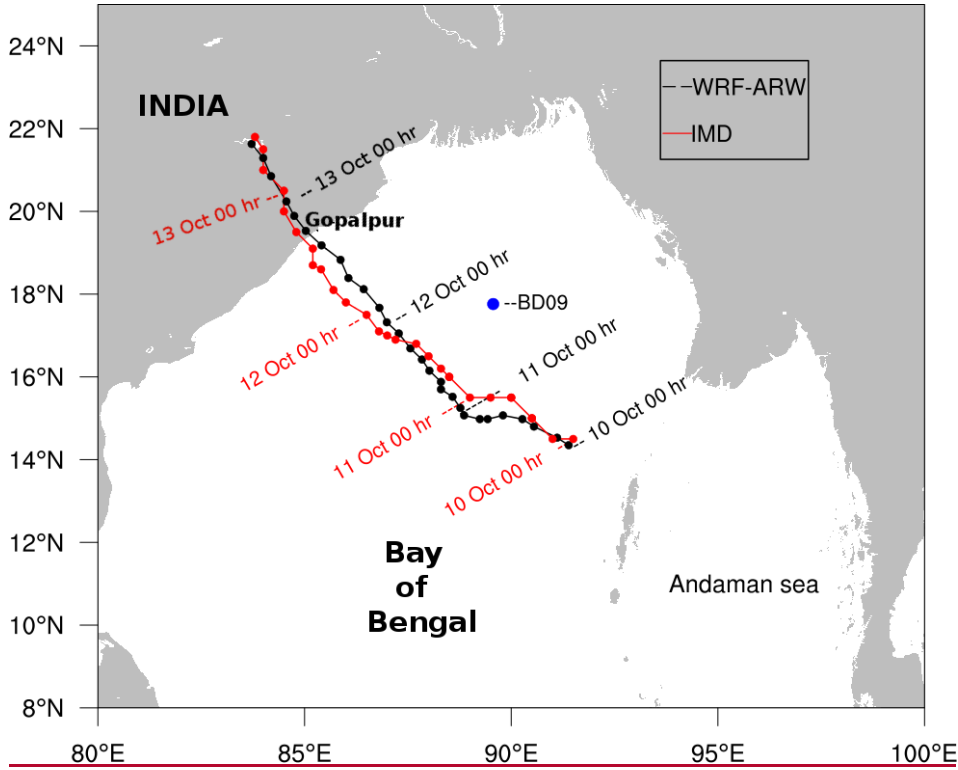


785
 786 **Figure 24:-COAWST model domain (65°-105 °E, 1°-34 °N) overlaid with GEBCO bathymetry (m).**
 787 **Locations used for time-series analysis are marked with a-stars.**

788
 789
 790



791



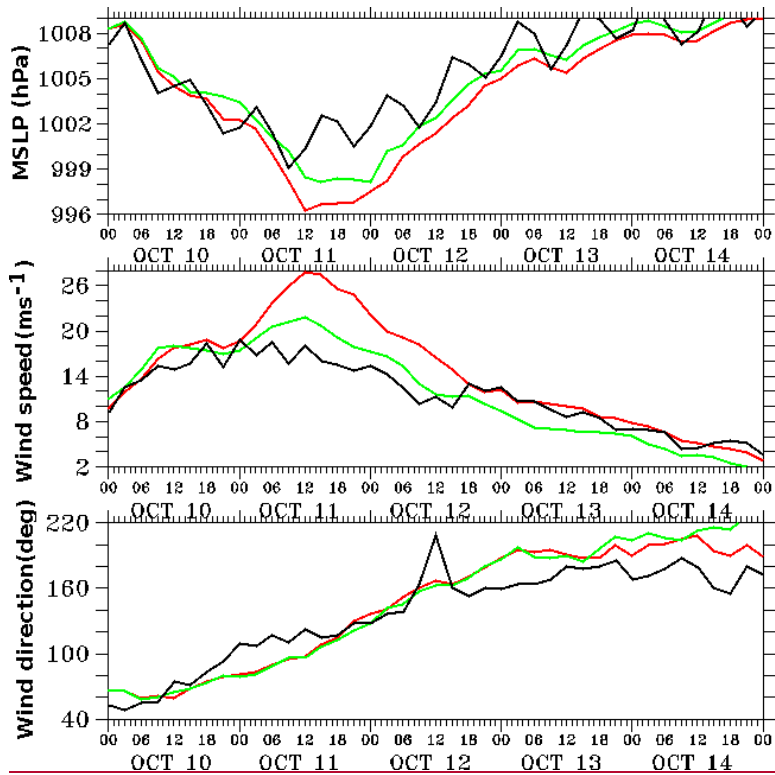
792 80°E 85°E 90°E 95°E 100°E

793 **Figure 32:- Validation of VSCS Phailin track simulated by coupled model (black) with IMD**
 794 **reported track (red). Tracks of Phailin simulated by the coupled model (black) and IMD reported**
 795 **(red). The 3-hourly positions of the center of Phailin marked with solid circles and the daily**
 796 **position at 00 hr are labelled with the dates. Location of buoy BD09 is marked with a blue circle.**

797

798

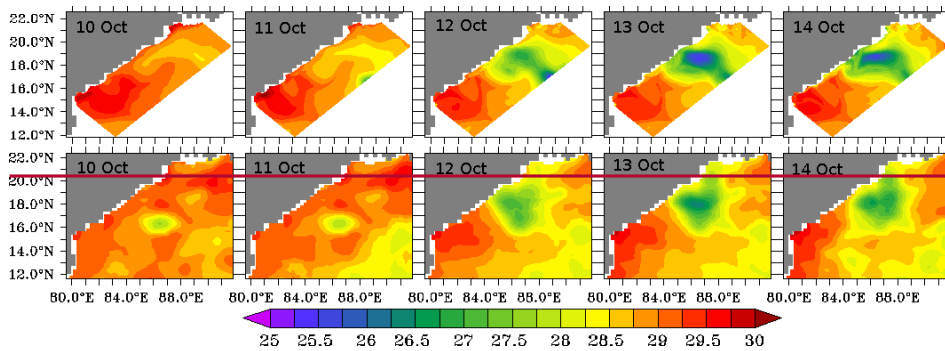
799



800

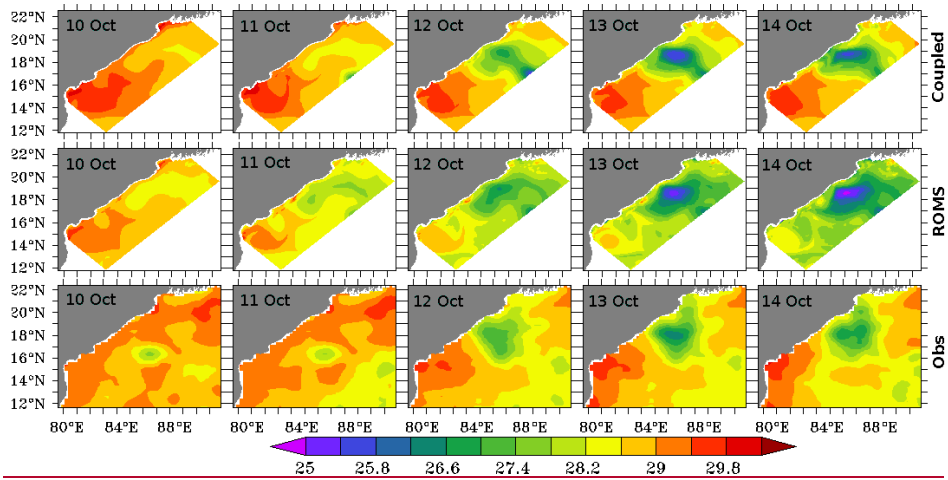
801 **Figure 4: Comparison of coupled model (green), stand-alone WRF model (red), and observations from a**
 802 **buoy BD09 (black) for the (top panel) mean sea level pressure (hPa), (middle panel) wind speed (ms^{-1}),**
 803 **and (bottom panel) wind direction (degree).**

Formatted: Superscript



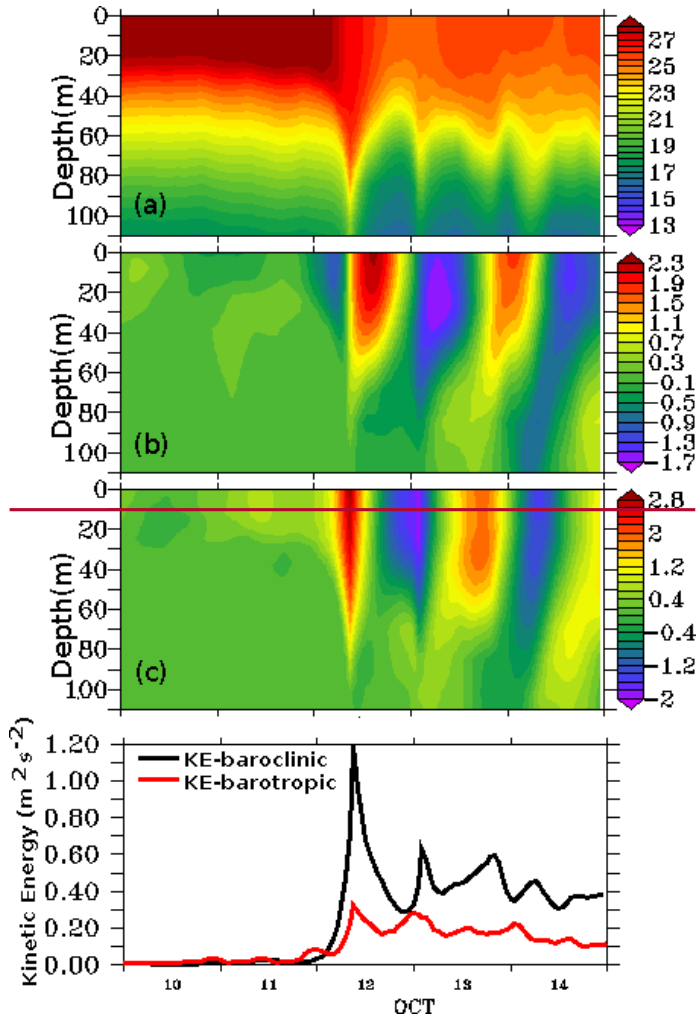
804

805



806

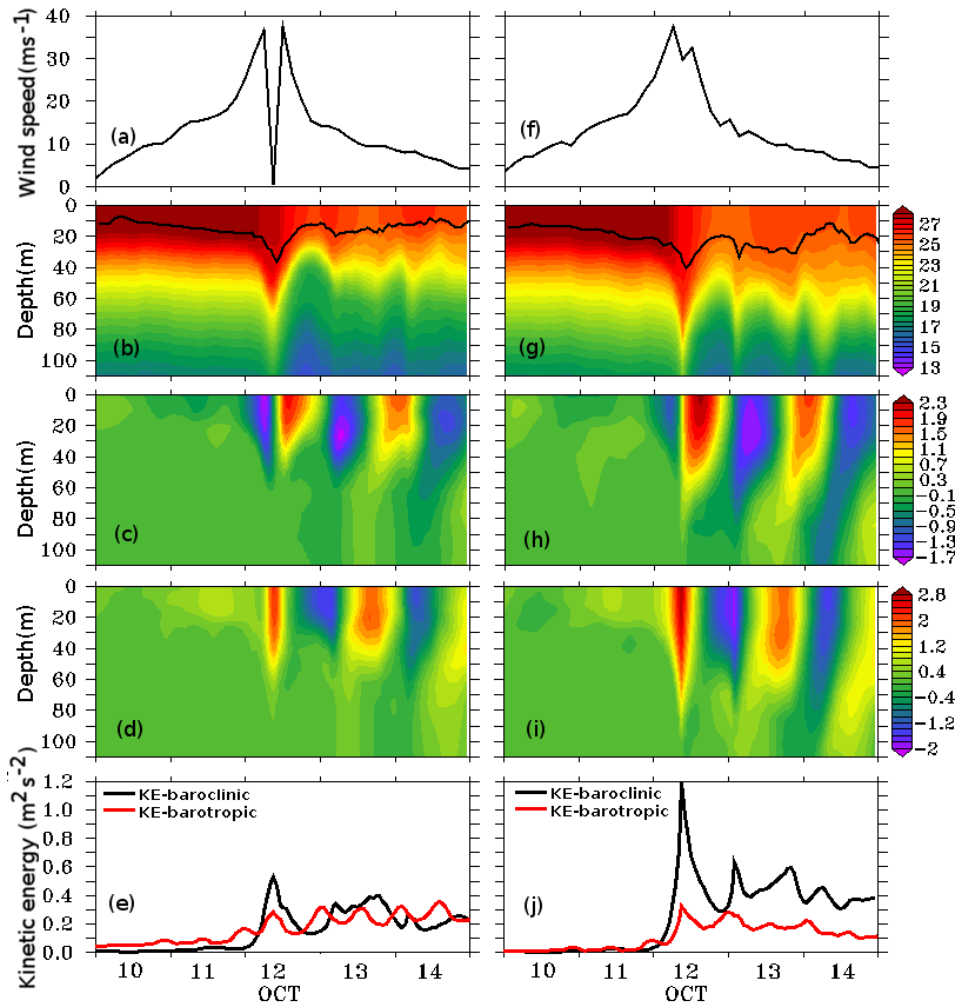
807 **Figure 53:- The daily averaged sea surface temperature Sea Surface Temperature (SST) in °C**
 808 **simulated by the coupled model (upper panel), stand alone ROMS model (middle panel), and**
 809 **observed from AVHRR sensor on the satellite (lower panel), and simulated by model (upper panel).**



810

811

812 **Figure 4: The vertical profiles of temperature in °C (a), zonal current in m s⁻¹ (b), meridional**
 813 **current in m s⁻¹ (c). The kinetic energy (m²s⁻²) of baroclinic current (black) and barotropic current**
 814 **($\times 10^{-3}$) (red).**



815

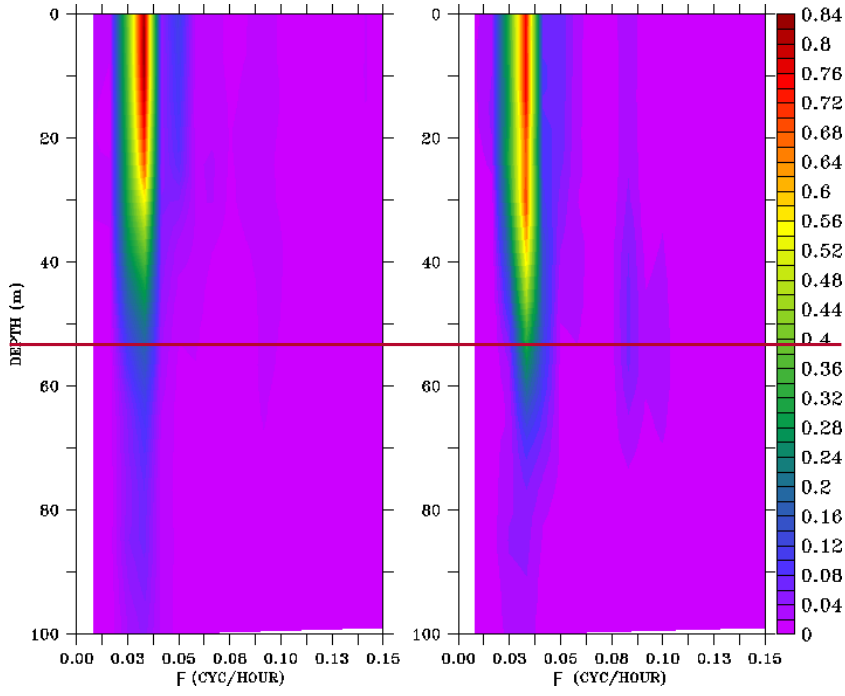
816 **Figure 6: Coupled model simulated and diagnosed variables at the on-track (left panel) and off-**
 817 **track (right panel) locations. (a, f) Surface wind speed (ms^{-1}), (b, g) temperature profile ($^{\circ}\text{C}$) and**
 818 **mixed layer depth (black line), (c, h) u-component of current (ms^{-1}), (d, i) v-component of current**
 819 **(ms^{-1}), (e, j) Kinetic energy of baroclinic (m^2s^{-2}) and barotropic ($\times 10^{-2} \text{m}^2\text{s}^{-2}$) current.**

820

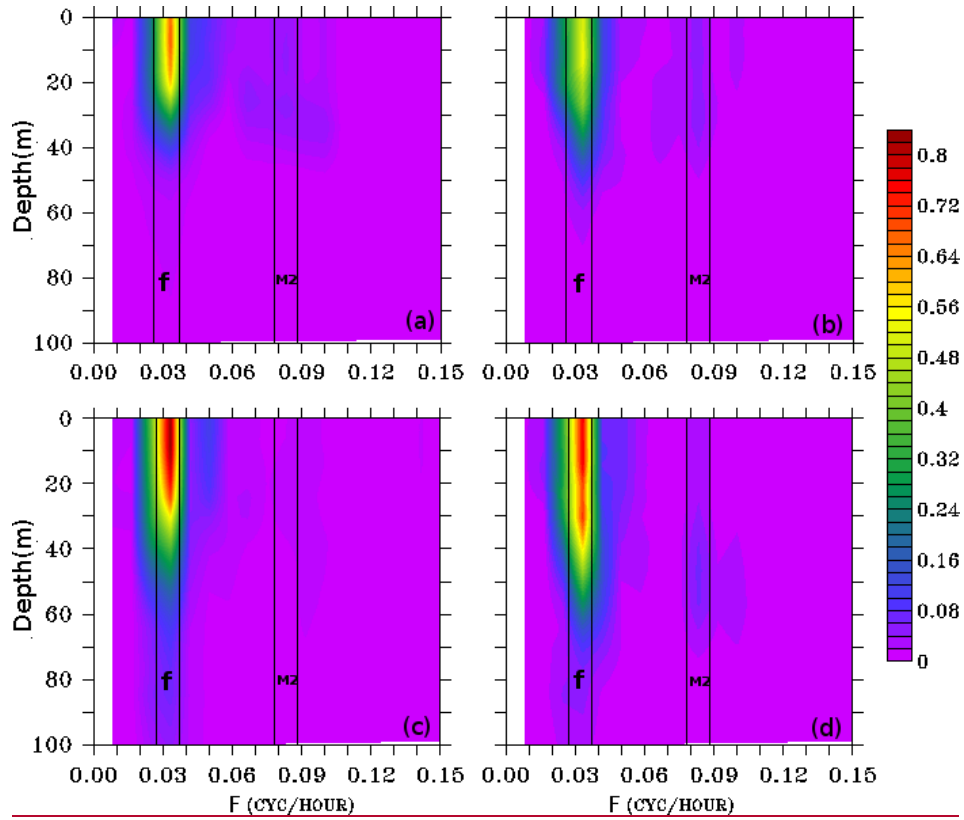
821

822

Formatted: Superscript

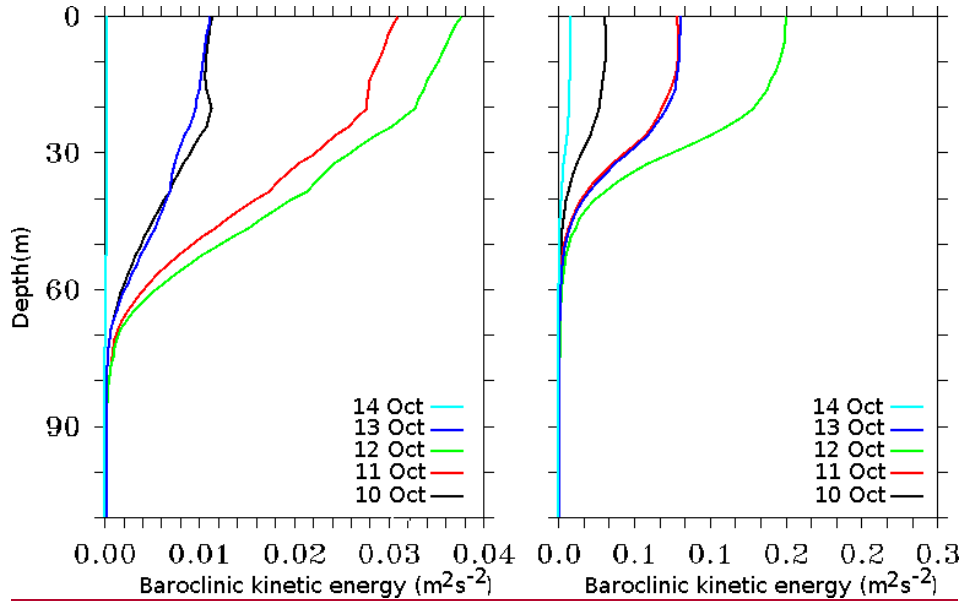


823



824
 825 **Figure 75:- The power spectrum analysis (m^2s^{-1}) performed on the simulation period at the on-track**
 826 **(upper panel) and off-track (lower panel) locations for (a, c) baroclinic zonal current and (b, d)**
 827 **baroclinic meridional current.**

828

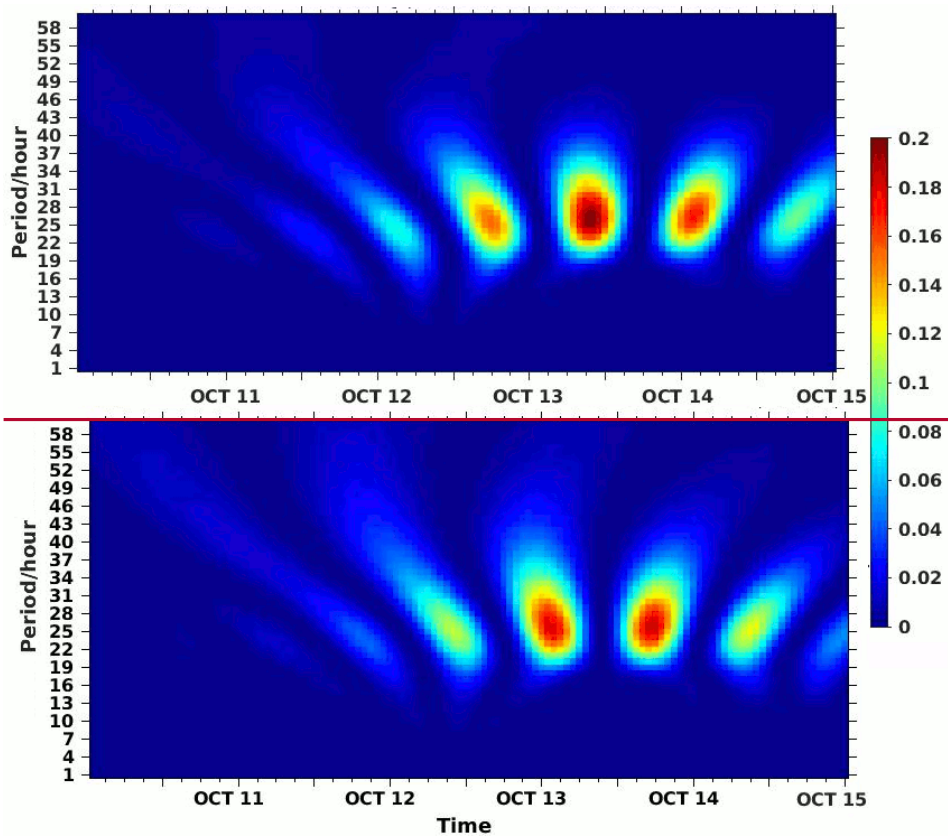


829

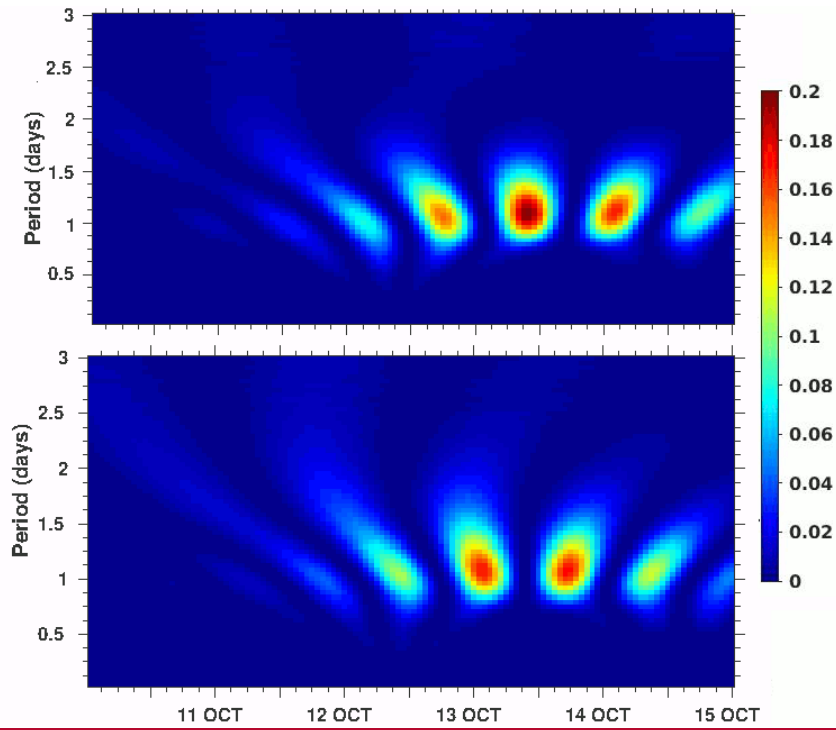
830 **Figure 8: Daily averaged baroclinic kinetic energy (m^2s^{-2}) profile at the on-track (left) and off-track**
 831 **(right) locations as marked with stars in Figure 2.**

Formatted: Font: Bold

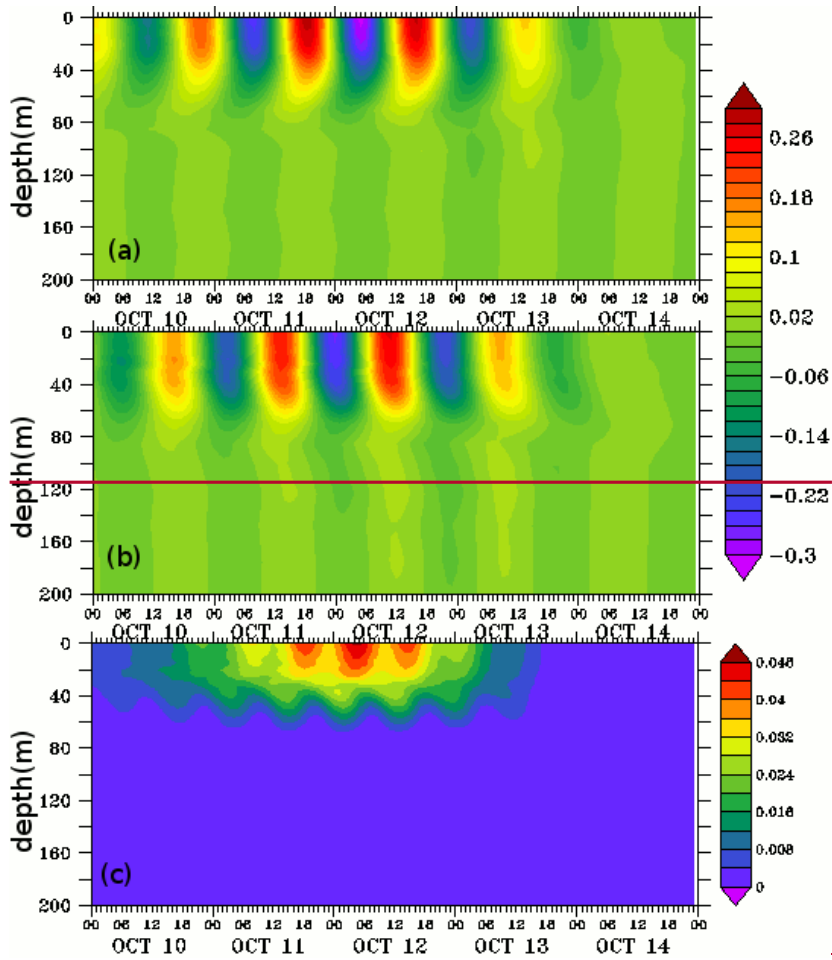
832



833

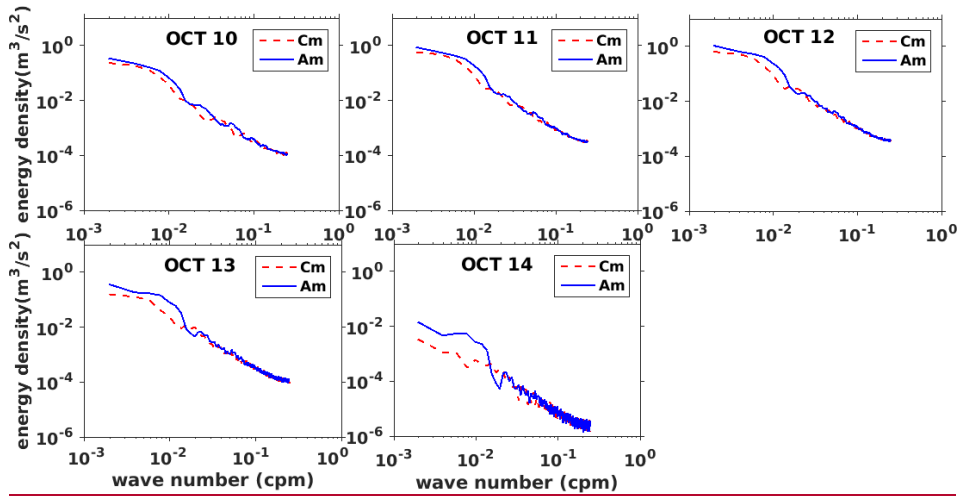
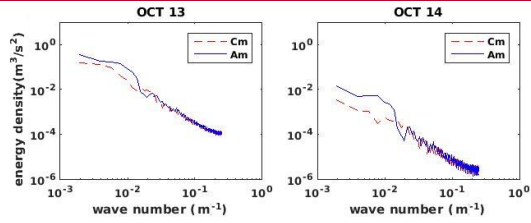
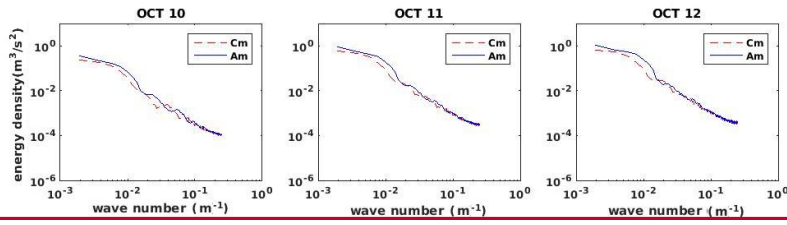


834
 835 **Figure 96:-** The scalogram in percentage at 40-14 m depth by continuous wavelet transform (CWT)
 836 method. Wavelet scalogram shown for the zonal baroclinic current (upper panel) and for the
 837 meridional baroclinic current (lower panel). **The white dashed line indicates the peak percentage of**
 838 **energy.**



839
840 **Figure 7: The profiles of a) near-inertial zonal baroclinic current (U_p) b) near-inertial meridional**
841 **current (V_p) in $m s^{-1}$ and c) Kinetic energy (E_p) of near-inertial flow in $m^2 s^{-2}$**

842
843
844
845
846
847

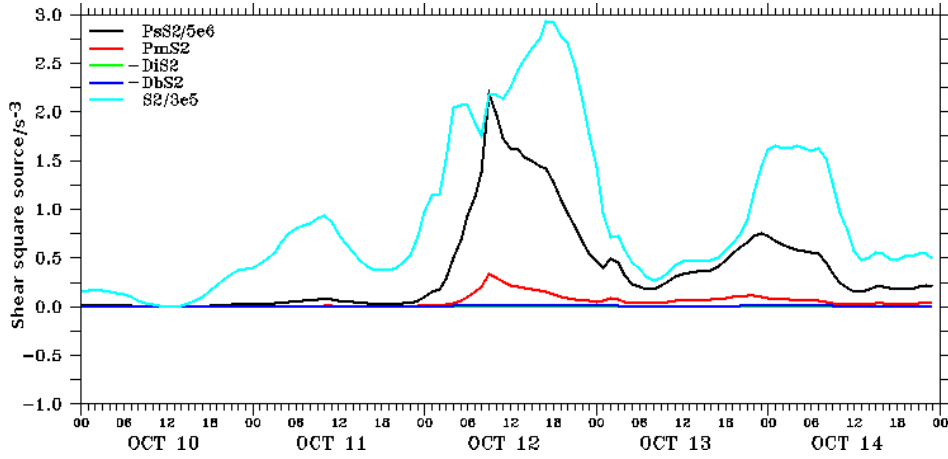


848

849

850 Figure 108:- The daily averaged vertical wave-number rotary spectra of near inertial oscillations.
 851 The anticyclonic and cyclonic spectra are represented in blue and dotted red lines respectively.

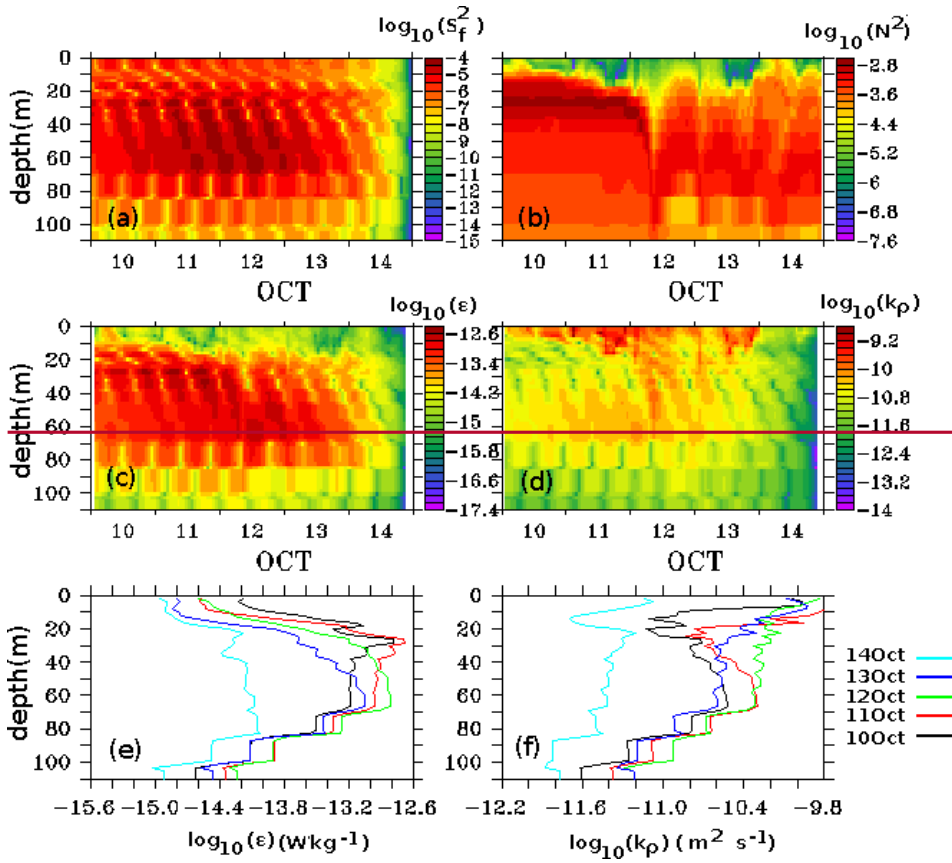
852



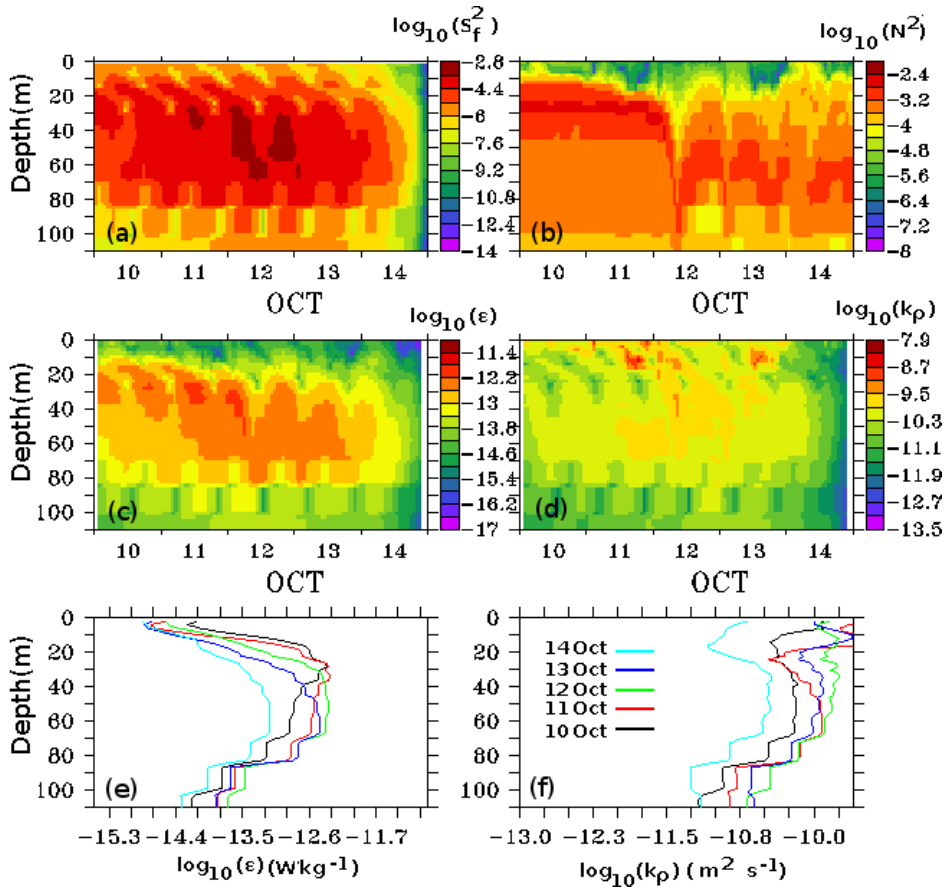
853

854 Figure 119:- The model simulated bulk properties at the selected point location. The vertical shear
855 square axis is multiplied with a factor of 10^{-6} . The magnitude of bulk shear squared S^2 (cyan color),
856 surface wind stress $P_s S^2$ (black color), barotropic effect $P_m S^2$ (red color), bottom stress $-D_b S^2$ (blue
857 color), interfacial friction $-D_i S^2$ (green color)

858



859



860
 861 **Figure 1210:- Profiles of (a) velocity shear $\log_{10}(S^2)$, (b) buoyancy frequency $\log_{10}(N^2)$, (c) turbulent**
 862 **kinetic energy dissipation rate $\log_{10}(\epsilon)$, (d) turbulent eddy diffusivity $\log_{10}(K\rho)$, (e) and (f) are daily**
 863 **averaged turbulent kinetic energy dissipation rate and turbulent eddy diffusivity respectively**

864